CROSS-SECTION MEASUREMENTS OF SC-43 AND V-48 RADIOISOTOPES PRODUCED VIA BERN MEDICAL CYCLOTRON

A THESIS SUBMITTED TO
THE GRADUATE SCHOOL OF NATURAL AND APPLIED SCIENCES
OF
MIDDLE EAST TECHNICAL UNIVERSITY

GAMZE SÖKMEN

IN PARTIAL FULFILLMENT OF THE REQUIREMENTS
FOR
THE DEGREE OF MASTER OF SCIENCE
IN
PHYSICS

JULY 2017

Approval of the thesis:

CROSS-SECTION MEASUREMENTS OF SC-43 AND V-48 RADIOISOTOPES PRODUCED VIA BERN MEDICAL CYCLOTRON

submitted by **GAMZE SÖKMEN** in partial fulfillment of the requirements for the degree of **Master of Science in Physics Department, Middle East Technical University** by,

Prof. Dr. Gülbin Dural Ünver _____
Dean, Graduate School of **Natural and Applied Sciences**

Prof. Dr. Altuğ Özpineci _____
Head of Department, **Physics**

Prof. Dr. Mehmet Zeyrek _____
Supervisor, **Physics Department, METU**

PD. Dr. Saverio Braccini _____
Co-supervisor, **Physics Department, University of Bern**

Examining Committee Members:

Prof. Dr. Osman Yılmaz
Physics Department, METU _____

Prof. Dr. Mehmet Zeyrek
Physics Department, METU _____

Prof. Dr. Altuğ Özpineci
Physics Department, METU _____

Prof. Dr. Meltem Serin
Physics Department, METU _____

Assist. Prof. Dr. Alper Hayreter
Dept. of Natural and Mathematical Science, Özyeğin University _____

Date: _____

I hereby declare that all information in this document has been obtained and presented in accordance with academic rules and ethical conduct. I also declare that, as required by these rules and conduct, I have fully cited and referenced all material and results that are not original to this work.

Name, Last Name: GAMZE SÖKMEN

Signature :

ABSTRACT

CROSS-SECTION MEASUREMENTS OF SC-43 AND V-48 RADIOISOTOPES PRODUCED VIA BERN MEDICAL CYCLOTRON

Sökmen, Gamze
M.S., Department of Physics
Supervisor : Prof. Dr. Mehmet Zeyrek
Co-Supervisor : PD. Dr. Saverio Braccini

July 2017, 74 pages

Positron Emission Tomography is a diagnostic technique in nuclear medicine to achieve quantitative measurements of biochemical processes in vivo, regarding its ability to detect positron-emitter-labeled radiopharmaceuticals at picomolar levels. An ideal PET radioisotope is required to have significant features decided by its half-life, decay kinematic, and cross-section. Thus, the ^{43}Sc radionuclide can be considered as a promising solution with its desirable half-life of 3.89 hours. The present thesis focuses on the production of ^{43}Sc by irradiating enriched-titanium TiO_2 with the 18 MeV medical cyclotron of Bern University Hospital and efficient measurements of the cross-section of the corresponding radioisotope. The proton current and energy on the target are optimized to result in expected cross-section values. As a part of this study, the vanadium radioisotope is produced via $^{nat}Ti\ (p,x)\ ^{48}V$ reaction with the solid target station that is recently installed in the Bern medical cyclotron. All steps applied for the ^{43}Sc production is followed to obtain ^{48}V radioisotope with the desired cross-section. Measurement of the cross-section is performed by gamma ray

spectroscopy, namely an outcome of a high purity germanium detector (HPGe). The result of the cross-section is represented as a function of proton energy and compared with both theoretical expectations and experimental values.

Keywords: Cyclotron, Radioisotope, Titanium, Scandium, Vanadium, Solid target station, Bern medical cyclotron laboratory

ÖZ

BERN MEDİKAL SİKLOTRONU KULLANILARAK ÜRETİLEN SC-43 VE V-48 RADYOİZOTOPLARININ TESİR KESİTLERİNİN ÖLÇÜMÜ

Sökmen, Gamze
Yüksek Lisans, Fizik Bölümü
Tez Yöneticisi : Prof. Dr. Mehmet Zeyrek
Ortak Tez Yöneticisi : PD. Dr. Saverio Braccini

Temmuz 2017 , 74 sayfa

Pozitron Emisyon Tomografisi, nükleer tıpta kullanılan ve canlı içindeki biyokimyasal değişimleri mikroskobik boyutlarda görüntülemeye izin veren bir teşhis yöntemidir. Bu amaçla kullanılan ideal bir pozitron-işaretli radyofarmasötiğin belirleyici özellikleri arasında, yarı ömrü, diğer parçacıklara bozunum kinematiği, ve tesir kesiti değerleri bulunmaktadır. Buna dayanarak, 3.89 saat yarı ömre sahip ^{43}Sc radyonüklidi arzu edilen bir aday olarak kabul görmektedir. ^{43}Sc'ün yarılanma ömrü bir yandan hücredeki anormallikleri gözlemleye yetecek kadar uzunken, diğer yandan işlem sonrası vücuttan hemen atılabilecek kadar da kısadır. Bu çalışma, IBA firmasına ait olan ve 18 MeV sabit enerjiye sahip Bern Üniversitesi medikal siklotronunda, zenginleştirilmiş titanyum (TiO_2) hedefinin proton ile bombardımanı sonucu elde edilen ^{43}Sc radyoizotopunun tesir kesitinin ölçülmesini amaçlamaktadır. Hedeflenen ölçümlerin gerçekleştirilebilmesi için ışınlama için kullanılan protonun üzerinde oluşan akım ve hedef üzerindeki enerji miktarı mümkün olan en iyi değerlerde tutul-

malıdır. Bu amaçla, normal şartlarda 18 MeV değerinde sabit olan siklotron enerjisi, farklı miktarlarda kullanılan ve de her biri 100 mikron kalınlığa sahip olan alüminyum levhaların yardımıyla daha düşük enerjilere kadar indirgenebilmektedir. Bu çalışmanın son aşaması olarak, $^{nat}Ti\ (p,x)\ ^{48}V$ reaksiyonu sonucu oluşan ^{48}V radyoizotopu yeni bir PET radyoizotopu adayı olarak üretilmektedir. Tesir kesiti ölçümü için gerekli olan verilere, yüksek saflıktaki germanyum detektörü (HPGe) kullanılarak elde edilen gama ışını spektromesi sayesinde ulaşılmaktadır. Sonuçlar, proton enerjisinin bir fonksiyonu olarak belirtilerek hem teorik beklentilerle hem de deneysel veriler ile karşılaştırılmaktadır.

Anahtar Kelimeler: Siklotron, Radyoizotop, Titanyum, Skandiyum, Vanadyum, Katı hedef istasyonu, Bern mekidal siklotron laboratuvarı

To my grandparents

Nazmiye Eken and Abdullah Eken

ACKNOWLEDGMENTS

I am more than grateful to my supervisor Prof. Dr. Mehmet Zeyrek. It has been an honor to work with him. He provided me an unparalleled guidance in my research and education. Under his supervision, I had the inspiration and freedom to discover my potential and exceed my limits.

I would like to thank to Prof. Dr. Antonio Ereditato, who gave me the chance to be a part of Bern University Albert Einstein Center for Fundamental Physics Laboratory for High Energy Physics group (AEC/LHEP). I feel myself privileged to work in the AEC/LHEP group. It was an excellent environment for the research and study.

I also greatly appreciate the support of my co-supervisor PD. Dr. Saverio Braccini. He always shared invaluable information and advises with me for my research. I could not have completed my thesis without his exceptional supervision and friendly guidance. Thank you for being patient and encouring me to improve myself!

I am grateful to Tommaso Carzaniga, Dr. Martin Auger, Dr. Konrad Nesteruk, and Maryam Mostafaei for their excellent collaboration, and generous contributions to my research. They always shared their knowledge and experiences with me to improve my study and to perform successful irradiations. I would like to thank Dr. Maruta Bunka for her supports during the gamma-ray spectroscopy and spectra analysis.

Many thanks to Turkish Atomic Energy Authority (TAEK) for the funding sources they provided during my master education.

A special mention goes to Peter von Ballmoos and Encarni Garcia Sanchez for being excellent hosts. I had a truly memorable time with you.

I would like to thank my colleagues and friends Canay Öz, Dilek Kizilören, Mustafa Elçi, Ali Murat Sözen, Çağlar Konak, Şahin Kürekci, and Buğra Bilin for always being there for me when I needed it. I really appreciate their friendship, and their

support.

Special thanks to Özgür Şahin for all his invaluable guidance, unconditional patience, and love. I am really lucky for having him in my life.

My final and special thanks go to my family, and my little swan Ípek for their continuous support and encouragement. I love you!

TABLE OF CONTENTS

LIST OF TABLES

TABLES

LIST OF FIGURES

FIGURES

CHAPTER 1

INTRODUCTION

Diagnosis and therapy are the main fields in nuclear medicine that require medical cyclotrons to produce affordable and efficient radionuclides. The invention of the cyclotron dates back to the late 30s, and since then, it has been the primary source for the radionuclide production. Therefore, installation of the cutting-edge medical cyclotrons, rarely equipped with a beam transport lines, are essential for the health centers dedicated to the nuclear medicine [16]. A radionuclide is necessary to perform PET measurements that allow to observe metabolic changes during the imaging process, to diagnose, and eventually to cure the diseases. The cyclotron produced radionuclides have become more crucial to achieve the measurements of possible biological abnormalities in vivo. Energy consumption of the tumor cells are relatively high comparing to the normal cells, and hence, a derivative of glucose, 2-^{18}F-fluoro-2-deoxy-D-glucose (FDG) is the most widely used conventional PET radiopharmaceuticals. It is highlighted by its slightly different structure from the glucose molecule, and thanks to this difference, FDG is partially consumed by the tumor cells. An ideal PET radioisotope can be categorized regarding its half-life and properties of the decay kinematics, especially the cross-section. The ^{43}Sc radioisotope is considered as a novel candidate for the PET technique with its remarkable properties. Particularly, its half-life of 3.89 hours is not only long enough to reveal possible abnormalities in the body cells, but also short enough to leave the body immediately after the imaging process is completed. It has also a low positron energy of 1.2 MeV, a high positron decay probability of 71$\%$, a low gamma ray emission energy of 373 keV, and a decay probability of gamma ray with 22.5$\%$.

The Bern medical cyclotron laboratory was constructed in order to fulfill both the production of PET radioisotopes and the scientific researches at the same time. The IBA Cyclone 18/18 HC medical cyclotron is installed with a 6 m-long Beam Transport Line (BTL) mounted on one of the extraction ports of the cyclotron. Although the cost of its installation is relatively high, the BTL is a significant factor to enable the multidisciplinary studies simultaneously [11].

The processes performed in this thesis are related to irradiation of the enriched TiO_2 target by proton beams to produce the ^{43}Sc radioisotope and to obtain the most efficient measurements of its cross-section. Time of the irradiation, current on the target, and energy of the proton beam should be optimized for the best results. However, the energy of the Bern cyclotron is fixed at 18 MeV. To overcome this constraint, aluminum absorber foils in various thicknesses are used to degrade energy of the proton beam, where the SRIM Monte Carlo code is used for the simulation of the degradation. On the other hand, the accelerator itself should be equipped with different types of target stations in order to access a large spectrum of radionuclides. For that purpose, the Bern medical cyclotron is equipped also with a solid target station. The ^{48}V radioisotope is produced via $^{nat}Ti\ (p,x)\ ^{48}V$ reaction. It has a half-life of 16 d, 50% of positron emission, and two high abundance gamma rays, one at 984 keV and the other at 1312 keV. After the irradiation process is completed, the target is cooled to be placed into a high purity germanium detector (HPGe). The obtained gamma ray spectrometry is used to calculate both activity of the irradiation and the cross-section. The results are represented as a function of the proton energy and the cross-section values.

The present thesis introduce nuclear medicine and imaging techniques in Chapter 2. Both the traditional and the modern methods are explained regarding their fields of utilization, working principles, and their comparisons with each other. Chapter 3 focuses on the medical cyclotron and their importance for the nuclear medicine. The working principle of a state-of-the-art-technology cyclotron is also described in detail. Chapter 4 provides a methodology for irradiation and for measurement of the cross-section. In other words, all information for the production of ^{43}Sc and ^{48}V are found in this chapter. Chapter 5 represents the all results for the different cross-section measurements and their comparison with the theoretical and the experimental values.

The theoretical data are obtained from TENDL (TALYS-base evaluation nuclear data library) whereas the EXFOR database is used for the experimental calculations. The interpretations and the discussions of the results are presented in this chapter.

CHAPTER 2

NUCLEAR MEDICINE AND IMAGING TECHNIQUES

Nuclear medicine and molecular imaging techniques are state-of-the-art-technologies, which have the ability to observe the abnormalities in picomolar quantities. They mostly provide a good prognosis by early detection of tumor cells or metastasis. Staging and treatment steps are other functions ensured by these tools. While the nuclear imaging techniques such as PET and SPECT provide physiological information of a specific organ or tissue, the traditional methods such as CT or MRI focuses only on the anatomical structure of the body [17]. During the imaging process, small quantities of the medical radioisotopes are used as an indicator to decide precise location of the tumor.

2.1 SPECT and Other Techniques

Single Photon Emission Computed Tomography (SPECT) is a nuclear imaging technique that aims to provide physiological information, such as the blood flow and metabolic activity in vivo with 3-dimensional distributions. Radio-pharmaceuticals are injected into the patient's body to label the tumor cell. In SPECT, gamma rays emitted by a radiotracer, are detected directly by the NaI(TI) scintillation detectors. The scintigraphic detections allow better localization compared to the other methods [18]. The basic working scheme for SPECT can be found in Figure 2.1.

Iodine-123 emits γ rays with an energy of 159 keV. This is ideally suited for imaging in the SPECT cameras, as they have been optimized for using with 99m Tc (γ ray energy =140 keV). For the SPECT agents, ^{99m}Tc is the most widely used accounting

for approximately 80 $\%$ of all studies in nuclear medicine. This is primarily due to its availability through the ^{99}Mo/^{99m}Tc generator [19].

Even though high possibility of obtaining low image quality in SPECT is a disadvantage for molecular imaging, some hybrid techniques, such as SPECT/CT can be seen as a promising solution. High image resolution of CT, and a wide variety of radiotracer sources dedicated to SPECT enable all required information about the tumor localization. These factors lead to a desired combination of both the anatomic, and the functional data [20]. As a traditional imaging method, Computing Tomography (CT) helps to receive anatomic information of the body to identify current diseases accurately. Its working principle bases on detection of the narrow beam x-rays produced by a rotating gantry around the patient. Inside of the gantry, there is an x-ray tube to shot the rays through the body. These rays are absorbed by the special x-ray detectors positioned on the opposite side of the source (Figure 2.2). After the detection, obtained information are immediately directed to computers for the data analysis with 2D image slices. The data is collected at various angles to make the image reconstruction accurate [4]. Another traditional imaging method, that uses the magnetic spins of hydrogen atom and align these spins like a compass under an external magnetic field, is Magnetic Resonance Imaging (MRI). Hydrogen atoms before and after the alignment are represented in Figure 2.3. The hydrogen atoms that are presented in the chemical structure of water and fat have unpaired protons and magnetic spins. These atoms are rotated by radio waves during the process, and simultaneously emit RF pulses, which are specifically binded to hydrogen. Consequently, detailed MR images of the tissues are created by these signals [5].

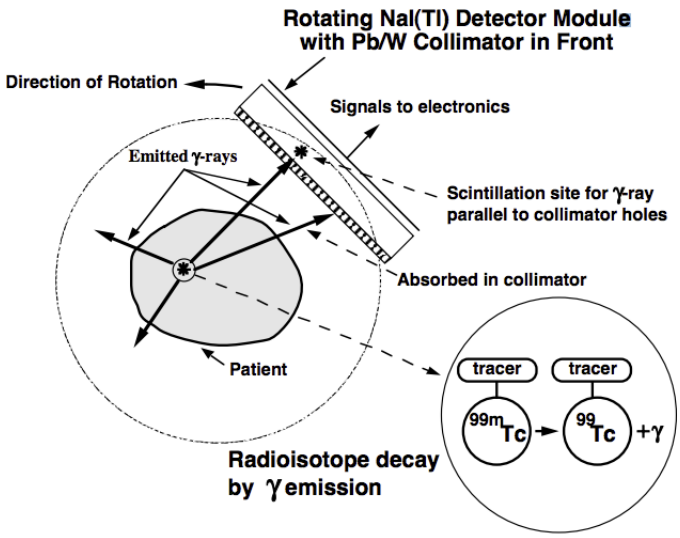

Figure 2.1: The working principle of SPECT [3]

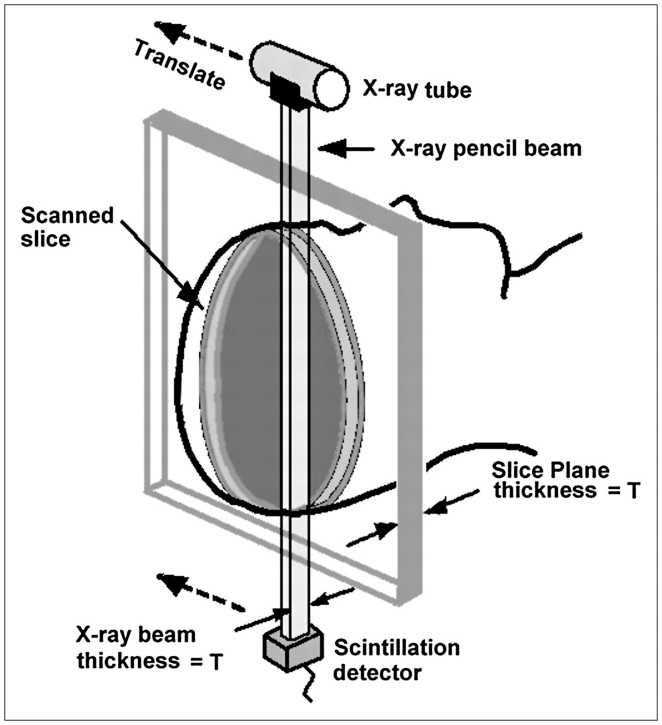

Figure 2.2: The working principle of CT and its X-ray tube [4]

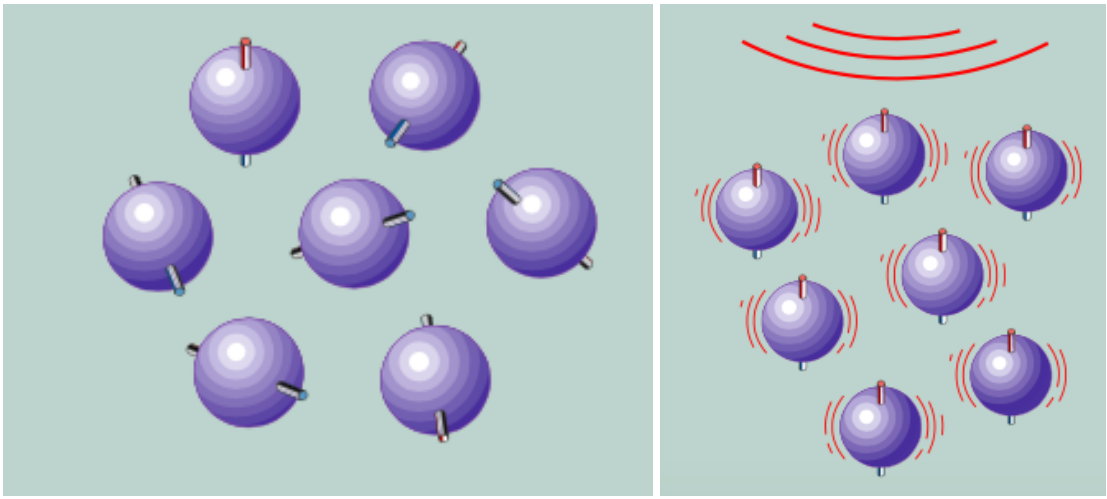

Figure 2.3: Hydrogen atoms in free space (left), and alignment of hydrogen atoms under a magnetic field (right) [5].

2.2 PET and Its Advantages/Disadvantages in Medicine

Positron Emission Tomography (PET) is utilized in a wide variety of clinical applications such as determining localization of the malignant tissues by using the non-metabolized radio-pharmaceuticals, and tumor imaging including brain, neck, head, and whole-body scans with a high accuracy. In other words, PET is not only used in the diagnosis of cancer tissues, but also plays a significant role in monitoring, staging and following steps after the therapy [21]. Epilepsy and Alzheimer are other illnesses that can be diagnosed by PET.

As the basic principle of this technique, positron-emitter molecules are injected into a vein to label the malignant cells for enabling observations of the biochemical functions [22]. It allows to detect tumor cells in the very early stages, and to prevent any possible metastases by estimating the spread rate of tumor cells easily. It also helps to distinguish the malignant and the benign tumors by providing enough staging information. By comparison with SPECT, PET provides more accurate results, image resolution with higher quality, and lower radiation exposure. Moreover, preparation and processing time for SPECT changes between 3 and 5 hours, which is quite long due to the low cost-efficiency rate. For instance, even though time required for the myocardial perfusion is 12 minutes in the SPECT scan case, the same process takes only 3.5 minutes with the ^{82}Rb-PET scan [6]. The images illustrated in Figure 2.4, belong the same patient, and clearly show the resolution differences between the

SPECT, and the PET images.

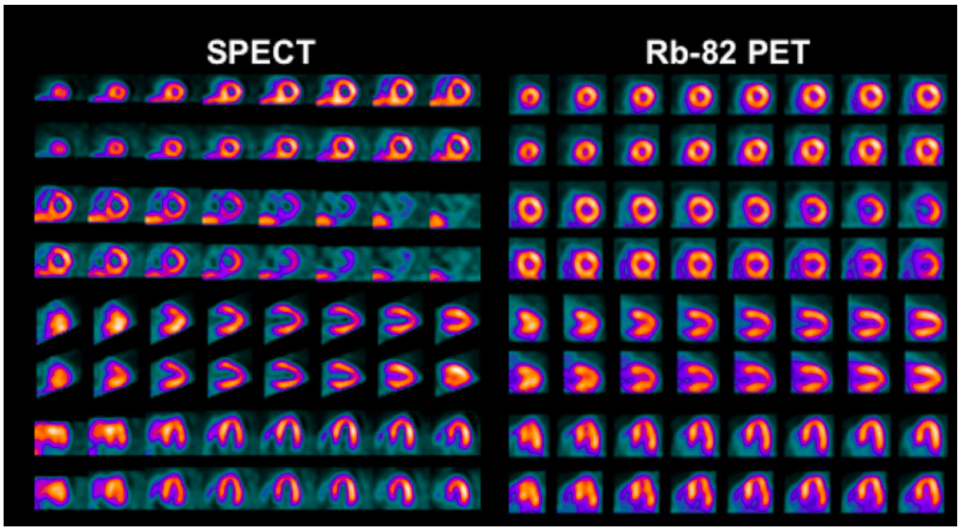

Figure 2.4: Comparison of the SPECT and the PET images [6]

Although it has many advantages, the applications of PET are limited due to availability of its radiotracers. In order to produce the PET radiopharmaceuticals, a medical cyclotron is required. However, installation of the cyclotrons are still not common in many medical centers because of its high cost.

2.3 The PET Radioisotopes

On the basis in the radionuclide production, structure of the target nucleus is modified after being bombarded by the charged particles. Characteristics of these charged particles, such as positron emission probability, and required energy to initiate a bombardment, have an influence on the possible outcomes of corresponding reactions [19]. Although fission reactions, occurred in the nuclear reactors, might be assumed as an alternative source for the radionuclide production, particle accelerator based radionuclides have a priority over other techniques. ^{11}C ($t_{1/2} = 20.3min$), ^{13}N ($t_{1/2} = 10min$), ^{15}O ($t_{1/2} = 2.03min$), and ^{18}F ($t_{1/2} = 110min$) are the four well-known positron emitting, and cyclotron-produced radionuclides. ^{11}C has a 100% positron decay with maximum β^+ energy of 968 keV. It is most commonly found in the forms of $^{11}CO_2$ and $^{11}CH_4$. ^{13}N decays to stable ^{13}C with 100% of positron emission as well, and can be produced by several reactions. However, its low half-

life and requirement of the enriched materials, to be used as targets, result in some limitations for its utility. The decay properties of the four common radioisotopes and the possible reactions are listed in Table 2.1.

Table2.1: Comparison of features of the four common radionuclides and their possible nuclear reactions, (a); These reactions required enriched target material. [1]

Radionuclide	$t_{1/2}$	Decay mode	Reaction	Energy (MeV)
^{11}C	20.3 min	β+	^{11}N(p,α)	11-17
^{13}N	9.97 min	β+	^{16}O(p,α)	19
			^{13}C(p,n)$^{(a)}$	11
^{15}O	2.03 min	β+	^{15}N(p,n)$^{(a)}$	11
			^{14}N(d,2n)	6
			^{15}N(p,n)$^{(a)}$	>26
^{18}F	110 min	β+	^{18}O(p,n)$^{(a)}$	11-17
			^{nat}Ne(d,α)	8-14

The most commonly used radio-labeled PET tracer is a glucose derivative, namely 2-^{18}F-fluoro-2-deoxy-D-glucose (FDG). It is obtained by replacing oxygen in the structure of glucose with ^{18}F (Figure 2.5). Since cancer cells grow at a high rate compared to normal cells, there is a direct relation between their energy demands and glucose consumption of the cells. This relation is named as 'metabolic trapping' [23]. Even though glucose is completely metabolized through the whole-body, glycolysis process is only possible for FDG up to a certain rate because of the ^{18}F labeling. This structural difference causes a high accumulation of FDG in cancer cells, and are detected as positive hot spots during the imaging step. Moreover, it has a desired half life of 110 min, which provides not only enough time for diagnosis after being injected into the patient, but also allows to remove the radioactive tracer from the body as soon as possible after the imaging process is completed. In addition, a long half-life enables fast and effective transportation between the production and the PET centers.

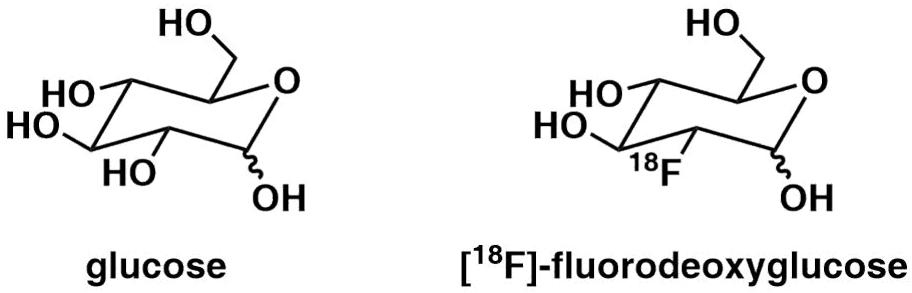

Figure 2.5: Difference of glucose and FDG [7]

2.3.1 Why Scandium is proposed as a new radioisotope

An ideal radioisotope should have a half life long enough to observe abnormalities of cells, and also short enough to leave the body as soon as possible after the imaging process. It also requires to be a good emitter of the gamma rays. Gamma rays are highly penetrating, and they are less ionizing than alpha and beta particles. Therefore, once they penetrate into patient's body, they give minimum damage. In addition, it should have a desirable production cross-section to obtain effective production yields. Regarding these properties, scandium might be considered as one of the most convenient choices with its ideal nuclear decay properties. It has a half-life of 3.89 hours, which is relatively long for both the diagnosis and the therapy purposes, with agreeable decay properties. Scandium may be labeled with either a positron-emitting isotope for the diagnostic purposes, or with a β^- particle for the therapy [16]. It is an 88.5$\%$ β+ emitter, and emits low energy gamma rays at 372.9 keV with the probability of 22.5$\%$ [24]. Besides that, the threshold energy to start the reaction is 3.142 MeV for $^{46}Ti(p,\alpha)^{43}Sc$, while it has a Q value of -3.0748 MeV [25]. Some decay properties of scandium radioisotopes are shown in Table 2.2. The decay percentages of each isotope are indicated in the parenthesizes.

2.4 Working Principles of PET

After injection of the corresponding radiotracer into the vein, the nucleus emits an energetic positron, known as positively charged electron. Subsequently, it travels a small distance through the tissue to encounter a free electron so that they collide,

Table2.2: Ground state properties of scandium isotopes (A < 45) [2]

Isotope	40	41	42	43	44
Type of decay	β+	β+	β+	β+	β+, EC
Half-life	0.18s	0.60s	0.68s	3.89h	3.92h
β end-point energy (MeV)	5.73 (50) 7.53 (15) 8.76 (15) 9.58 (20)	5.61	5.39	0.80(23) 1.19(77)	1.47 (99)
γ's following β+ decay (MeV)	0.73(41) 1.11(7) 1.83(24) 2.02(22) 3.19(13) 3.73(100) 3.92(18)			0.375(100)	1.156 (100) 1.500 (0.8) 2.656 (0.14)

and produce an unstable positronium. As a consequence, the collision ends with an annihilation process, where a photon pair is formed with individual energies of 511 keV (the rest mass of electron and positron). These photons are the gamma ray signals moving in the opposite direction, and they are detected by the ring-shaped PET scanners (Figure 2.6). While the ring-shaped detectors help to collect data with a wide range of angles through the related organs, having a simultaneous detection of photons is essential to be counted as an event. It is provided by the collinearly aligned detectors, and obviously, this detector technology allows PET to be a highly sensitive device compared to the other imaging techniques [22]. The varying positions of the radioactive source are computed in slices, and recorded as 3-D images of the tissue [8]. Nevertheless, estimation of the tracer location is not very accurate, since the positron travels for a while before resulting in an annihilation; i.e. turning into photons. This location uncertainty might be considered as a reason for possible errors in the imaging [26].

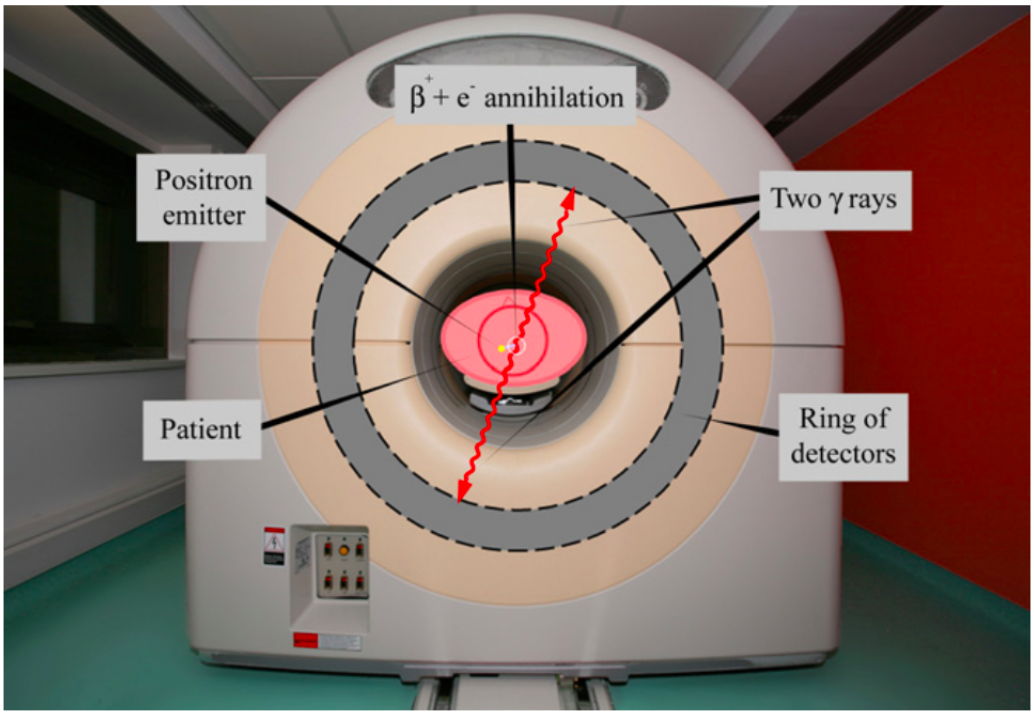

Figure 2.6: Proton-electron annihilation and detection of photons by the ring-shaped detectors [8]

2.5 The PET/CT Technique

Even though the data provided by PET is crucial for diagnosis, staging, and treatment planning, improvements in the precision of the measurements are still required to obtain more accurate results. In order to provide this, the PET/CT scanner plays an innovative role as a hybrid technology in the nuclear medicine, which contains of both the CT and the PET devices mounted in the same gantry. After the signals provided by PET are converted into real images, and analyzed, CT information are computed to finalize the process. First PET/CT device was constructed in 1998 by CTI PET Systems in Knoxville, Tennessee, the company named as Siemens Molecular Imaging now. After it was installed at the University of Pittsburgh (Figure 2.7) [9], it has started to gain a remarkable repetition in the efficient diagnosis all around the world. Indeed, it combines both the functional data of PET and the anatomical information of the x-ray CT scanner. This combination allows to determine localization of the tumor in early stages even if they cannot be seen as a structural change in the body. More precise detections of small abnormalities are also possible by highlighting the

FDG-accumulated organs (Figure 2.8) [23].

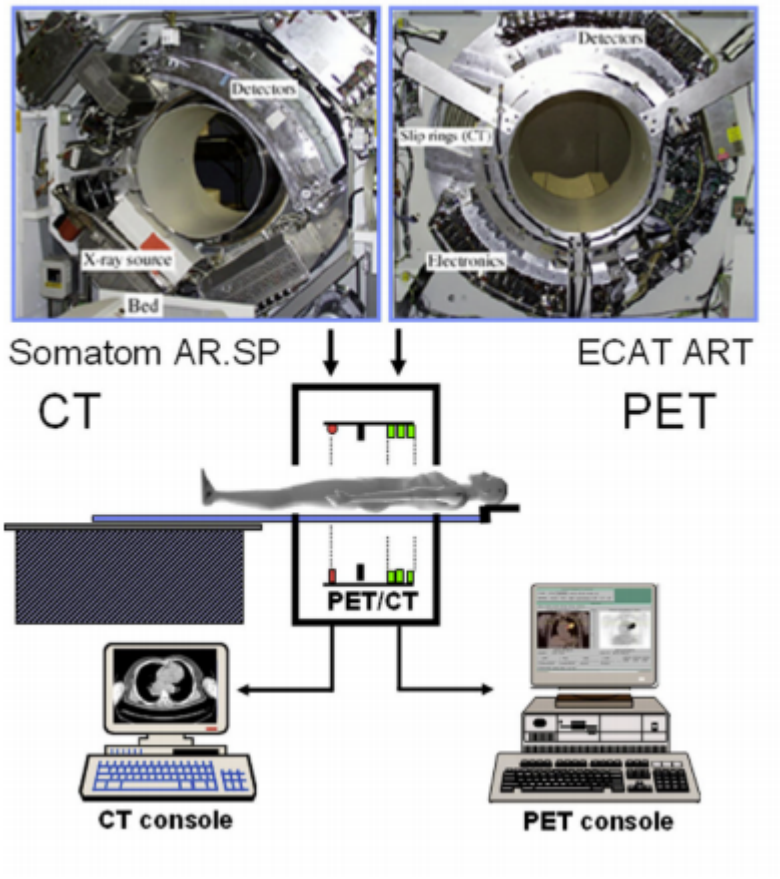

Figure 2.7: The first PET/CT prototype design evaluated clinically at the University of Pittsburgh. The CT and PET components were mounted on a single rotating support and the data acquired from two separate consoles; the CT images were transferred to the PET console and then used for CT-based attenuation correction and localization [9]

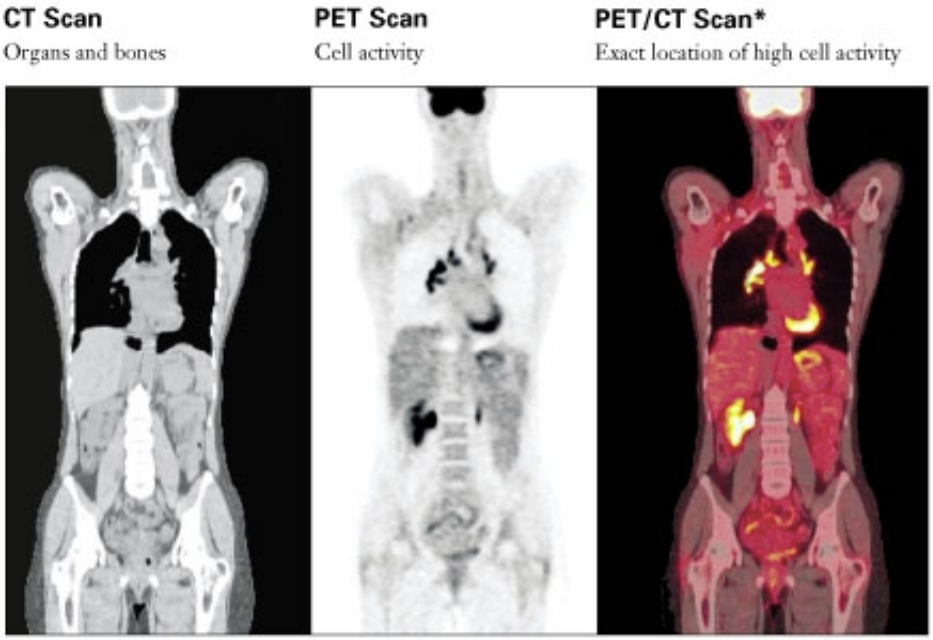

Figure 2.8: Comparison of CT, PET and PET/CT Scans [10]

CHAPTER 3

MEDICAL CYCLOTRONS

Cyclotron was conceived in Berkeley, U.S.A. in the beginning of 1930s, due to a need arose from generating high speed ions without using of high voltages [27]. Ernest Lawrance and Milton Livingston accelerated ions of the hydrogen molecule to the energy of 80 keV with a 100 mm pole cyclotron in 1931. An improved version of the cyclotron accelerated protons to the energy of 1.22 MeV and deuterons to the energy of 3.6 MeV in 1932[28]. A high-speed deuteron beam was collided with a carbon target in order to form a short-lived radioisotope. Hence, a new and safe way of obtaining radioisotopes was found. A few years later from the discovery of these machines, E. Lawrance's brothers used Phosphorous-32 for leukemia [13]. This was the first step to use the cyclotron-produced radioisotopes for medical purposes. Since then, these short-lived and proton-rich radioisotopes are being extensively used in medicine for both diagnostic and therapy purposes. In 1941, the first cyclotron for medical purposes was installed at Washington University to produce radioisotopes of phosphorus, arsenic, iron, and sulphur [29]. The medical cyclotrons are placed mostly in hospitals, universities with the aim of research and development, and companies that both produce and sell these radionuclides. Cyclotrons with rapidly developing technologies are offering a wide range of applications today. Biomedicine, biology, pharmacology, agriculture, and geology are some important fields, which use radionuclides as tracers [30].

3.1 The Bern Cyclotron

As previously mentioned, medicine has two important fields; diagnosis and therapy. These fields are substantially related to use of particle accelerators and detectors. On this basis, a project, named as SWAN (Swiss hAdroN), was built by a collaboration of the Bern University Hospital – the Inselspital – and the University of Bern in 2007 to combine radioisotope production, proton therapy, and multi-disciplinary researches. The Bern cyclotron laboratory was constructed underground, and it contains an IBA Cyclone 18 MeV cyclotron. The cyclotron can be regarded as the heart of the SWAN project to produce the PET radioisotopes for both industrial, and scientific aims (Figure 3.1). Apart from the cyclotron, there is a beam transport line (BTL) terminating in a different bunker to carry out production and research at the same time [31]. SWAN also includes radiochemistry and radiopharmacy laboratories, and two floors are dedicated to the treatment of the oncological patients and to nuclear medicine researches.

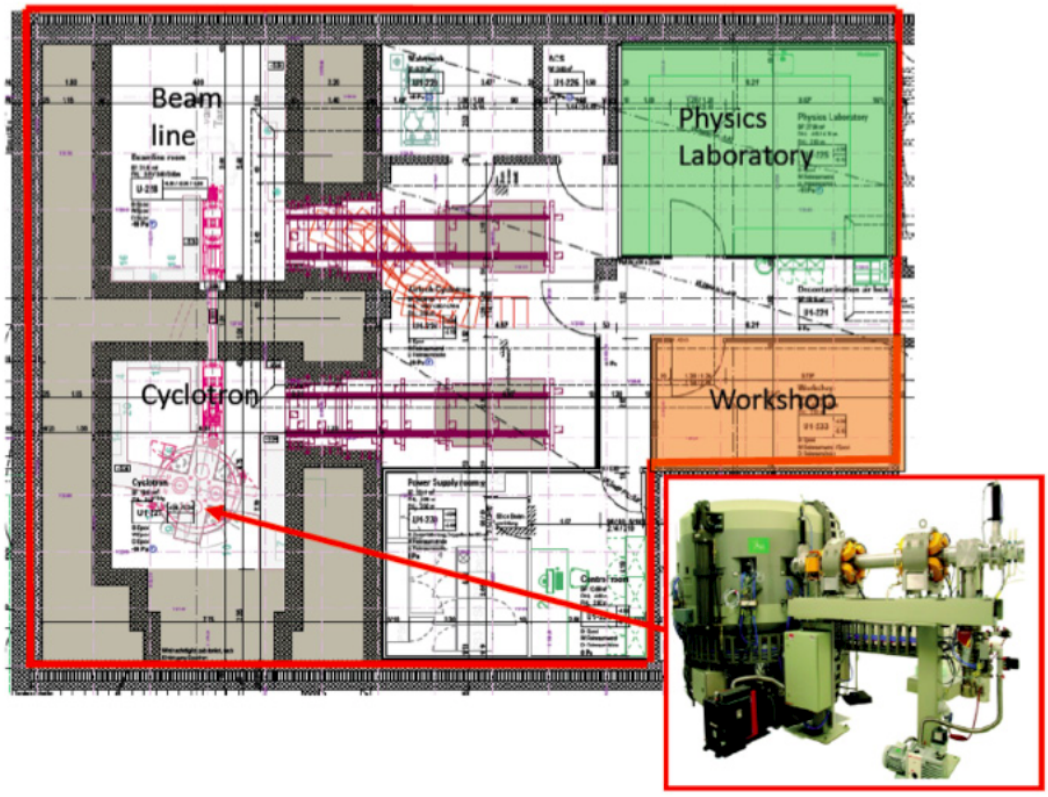

Figure 3.1: Scheme of the Bern Cyclotron Laboratory and location of the Cyclotron

Table3.1: Main characteristics of the Bern Cyclotron and the BTL

Constructor	Ion Beam Applications (IBA), Belgium
Type	Cyclone 18/18 HC
Accelerated particles	H^- (D^- on option)
Energy	18 MeV (9 MeV for D^-)
Maximum current	150 μA (40 μA for D^-)
Number of sectors	4
Angle of the dees	30°
Magnetic field	1.9 T on the hills and 0.35 T on the valleys
Radio frequency	42 MHz
Weight	24000 kg
Dimensions	2 m diameter, 2.2 m height
Ion sources	2 internal PIG H^-
Extraction ports	8 (one of which connected with the BTL)
Extraction	Carbon foil stripping (for single or dual beam)
Strippers	Two per extraction port on a rotating carrousel
Isotope production targets	4 $^{18}F^-$, ^{15}O (^{11}C and solid target are foreseen)
Beam Transport Line (BTL)	6.5 m long
	two quadrupole doublets (one in each bunker);
	XY steering magnet; upstream collimator;
	2 beam viewers; neutron shutter

IBA Cyclone 18/18 HC provides an energy of 18 MeV with a maximum of 150 μA extracted current. Moreover, it contains two different H^- ion sources to ensure continuity of the production process with the second source if any problems arise in the other source. It also has eight different extraction ports; four for fluorine-18, one for solid target station, one foreseen for carbon-11, and one for BTL. The four liquid targets dedicated to ^{18}F take place so that they can be used in case of any maintenance or any possible need without disturbing current production. Further technical details on the Bern cyclotron and BTL are reported in Table 3.1.

3.1.1 The Beam Transport Line

Beam Transport Lines generally are not common in medical cyclotrons. In situations, which they are combined with the cyclotrons, they share the same bunker. This common use situation prevents the possibility of both production, and research at the same time. In the Bern cyclotron laboratory, there is a specific Beam Transport Line (BTL)

(Figure 3.2) to eliminate this negative consequence, and allows to study in multidisciplinary research fields such as production and development of PET radioisotopes, material sciences, and radiation protection in parallel.

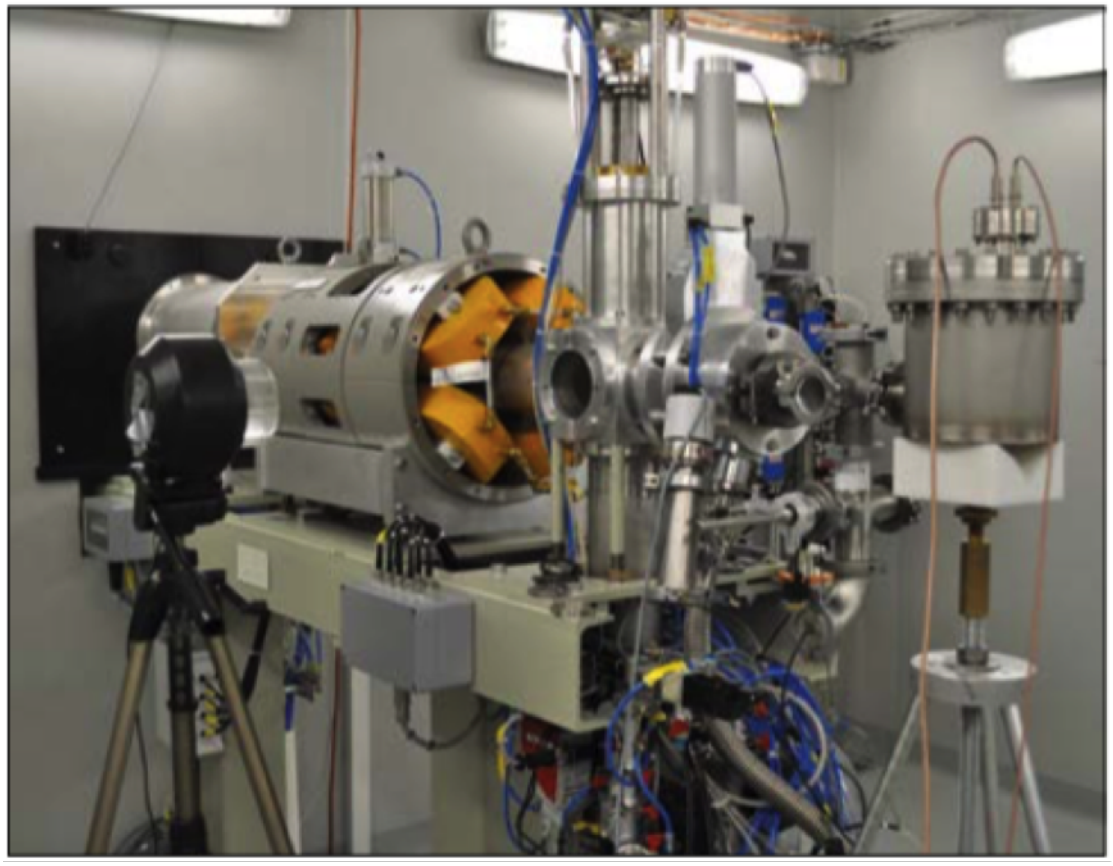

Figure 3.2: The BTL and the bunker that is dedicated to the BTL

It is 6.5 m long, and allows production of radioisotopes at high currents up to 150 μA with more than 95$\%$ transmission. This high transmission is important to avoid any corrosion occurred on the radiation sensitive devices, and any possible activation caused by undesired sub-interactions. Hence, different methods have been applied in the design of BTL to enable the maximum high transmission. One method is centering the beam through the beam line path. Although it has a curved shape inside of the cyclotron, the beam must follow a straight path along the beam line. An XY steering magnet is placed near to the extraction point of the beam to obtain a straight path as much as possible. Using two different H-V quadrupole doublets is another method for observing a precise beam path. These doublets improve the horizontal and the vertical alignment of the beam. While the first doublet comes immediately

after the X-Y steering magnet placed in the first bunker, the second one is located in the other bunker reserved for BTL. Beam viewers and collimator are also help to position the beam. All these apparatus ensure the maximum transmission during the production. Furthermore, a wall with thickness of 180 cm is placed between the first and the second bunkers, and a neutron shutter is mounted on BTL in order to increase the transmission rate [11]. A detailed scheme of the BTL is available in Figure 3.3.

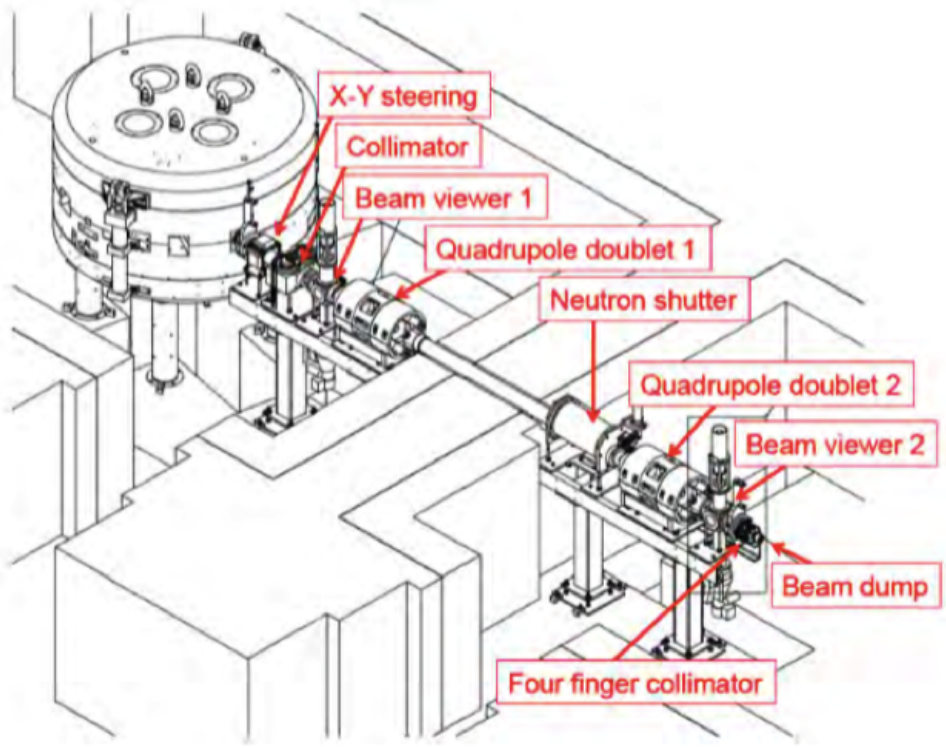

Figure 3.3: A detailed scheme of the BTL and descriptions of its parts [11]

3.2 Working Principle and Construction

Cyclotrons use the magnetic field to drive charged particles in a circular path, while they use electric field to accelerate the corresponding particles. As mentioned previously, the main aim of a cyclotron is accelerating particles up to possible high energies. Hence, direct proportionality between velocity and energy of the accelerated particle is the basic factor that affects the process [1]. In the cyclotron, there are two large electromagnets in order to create perpendicular magnetic field. Between these two poles, there is a vacuum chamber, that involves an ion source at its center, and two

hollow D-shaped electrodes called dees. When a high frequency alternating voltage is applied to an ion, which is already produced by ion source, this charged particle starts to be accelerated through the dees. It follows a semi-circular path under the magnetic field, and then comes back to the gap between dees (Figure 3.4).

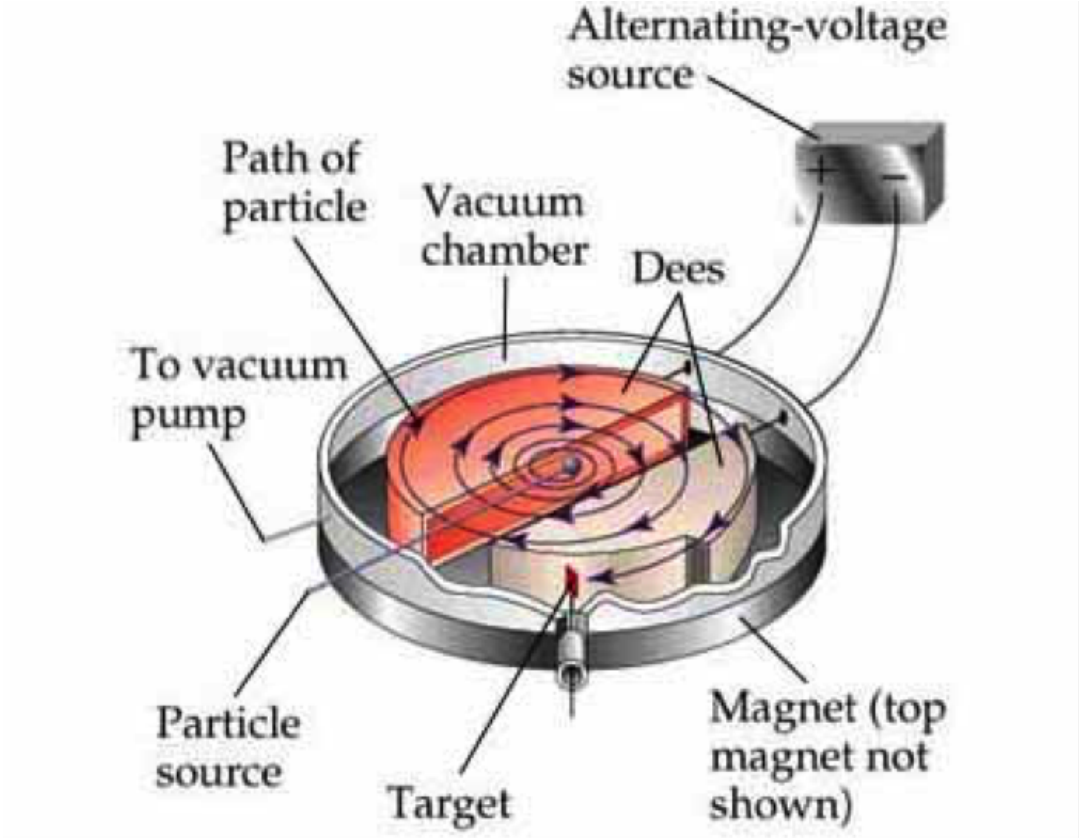

Figure 3.4: A schematic representation of the cyclotron [12]

Meanwhile, electric field in the gap is continuously reversed to give the charge a further acceleration so that it could enter to other dee, and gain more energy. The time taken for the charged particle to finish its path in one dee has to be equal to half time period of the alternating voltage source. Thus, the polarity of the dees changes just in time when the charged particle reaches the gap [32]. Otherwise, acceleration cannot occur. As the acceleration continues, radius of the circular path becomes gradually larger until reaching the outer surface of dees. In the end, the charged particle, which already has a high velocity and high energy, is emerged from the cyclotron by passing through a narrow line with a high electric field across it. The final energy of extracted particles is directly proportional to square of both magnetic field, and final radius of the circular path. Hence, energy of the particle becomes higher and higher as size of

the magnets increases [33]. Charge, amplitude of the potential difference, and phase relationship between the particle and the electric field are the other factors that affect the final energy [1]. On the other hand, rotational frequency of the cyclotron does not depend on the orbital radius, as it is proportional to the magnetic field, and to the charge. A schematic representation of the cyclotron can be found in Figure 3.5.

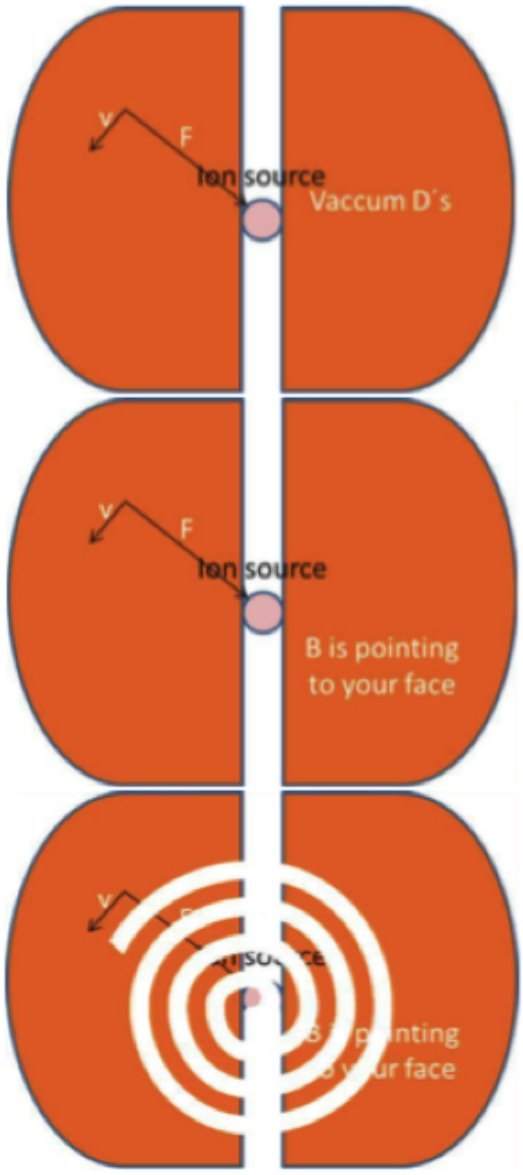

Figure 3.5: Cyclotron schematics: from top to bottom; ion input location, $\vec{F} = \vec{v} \times \vec{B}$, and ion path [13].

It is already known that magnetic and electrical fields play an important role in the

acceleration of particles. Formula for the cyclotron force under these fields can be written in the vector form as follows:

$$\vec{F} = q(\vec{E} + \vec{v} \times \vec{B}), \tag{3.1}$$

where q is the charge of the particle, υ is the velocity of the particle, B is the magnetic field, and E is the electric field. The force that moves particle in an orbital path is expressed as:

$$\vec{F} = q(\vec{v} \times \vec{B}), \tag{3.2}$$

or in the scalar form as:

$$F = q\upsilon B. \tag{3.3}$$

Moreover, the central force for a particle that follows a circular path can be described as:

$$F = \frac{m\upsilon^2}{R}, \tag{3.4}$$

where m is the mass of the particle, and R is the radius of the path. It is quite obvious that, these two forces can be equaled to each other as:

$$q\upsilon B = \frac{m\upsilon^2}{R}. \tag{3.5}$$

By this equality, it can be easily seen that:

$$\upsilon = \frac{qBR}{m}. \tag{3.6}$$

Kinetic energy of the particle is also known as:

$$KE = \frac{1}{2}mv^2. \tag{3.7}$$

If Eqn. 3.6 is put into Eqn. 3.7, the kinetic energy becomes

$$KE = \frac{q^2B^2R^2}{2m}, \tag{3.8}$$

which is directly proportional to square of the charge, the magnetic field, and the radius as it was mentioned before. Moreover, in the cyclotron, the particle has also an angular velocity as well as a linear velocity. The relation between these two velocities are written as follows:

$$v = wR, \tag{3.9}$$

where ω is the angular velocity and can be formulated with respect to the cyclotron frequency of the motion as:

$$\omega = 2\pi f_c. \tag{3.10}$$

As a further step, the linear velocity can be written in terms of the cyclotron frequency by:

$$v = 2\pi f_c R. \tag{3.11}$$

Finally, if Eqn. 3.6 and Eqn. 3.11 are combined, the cyclotron frequency is obtained as:

$$f_c = \frac{qB}{2\pi m}, \tag{3.12}$$

which is totally independent of the orbital radius, R.

In cyclotrons, particles travel near to the speed of light due to their high energies. Hence, the mass formula should be modified in relativistic form;

$$m = m_{\circ}\gamma, \tag{3.13}$$

with

$$\gamma = \frac{1}{\sqrt{1-(v/c)^2}}, \tag{3.14}$$

where c is the speed of light.

The cyclotron frequency formula are modified for these relativistic particles as:

$$f = \frac{f_c}{\gamma}, \tag{3.15}$$

and it is rewritten with Eqn. 3.12,

$$f = \frac{qB}{2\pi\gamma m_0}. \tag{3.16}$$

3.2.1 Extraction of the Beam

For all accelerators, extraction of the beam efficiently plays an important role. Although extraction generally causes no problem for linear accelerators, and this might be accepted as one of the most important advantages of them, it is not possible to say the same thing for the cyclotrons. The H^- and the D^- sources are usually used to produce the PET radioisotopes [34]. The extraction by stripping is the most common way of the beam extraction (Fig 3.6, left), and it is generally performed by the H^- cyclotrons. The method is based on placing a thin foil in front of the beam, and then stripping the electron at the extraction radius by hitting this foil. After stripping, only positively charged particles remain. They are affected by the magnetic field in opposite direction, and then released out of the cyclotron. In the H^+ cyclotrons, an electric or local magnetic field is used to extract positive ions by deflection (Fig 3.6, right) [32]. Radial position of the foil can be adjusted at different angles during the magnetic field applied, and it enables a bombardment at a large energy range [35].

Moreover, stripping extraction allows to reach higher currents (300 μA - 500 μA) during the irradiations, that leads to an extraction with almost 100% efficiency and to a minimum internal interaction with the cyclotron components. Besides, simultaneous extractions might be achieved if two different foils are available i.e., a coincidence production of two different radioisotopes at different beam currents is possible [34].

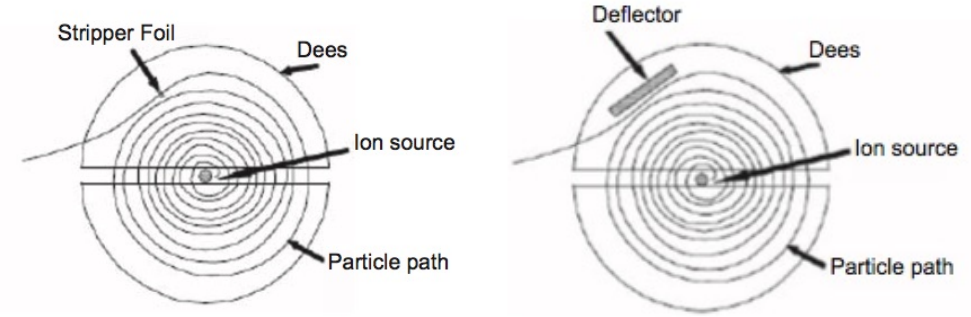

Figure 3.6: Extraction by stripping (left), and extraction by deflection (right) [1]

3.3 Principles of the Radionuclide Production

Reactions occurred in the nuclear reactors, and bombardment of the charged particles by using accelerators are two main methods to obtain various radioisotopes for medical purposes. In order to carry out a reaction, distance between two nuclei must be short enough, and amount of the energy to overcome the barrier must be provided. This barrier is a result of the natural electromagnetic repulsion between protons and, named as the $Coulomb\ barrier$. Magnitude of the Coulomb barrier can be assumed as the amount of kinetic energy to keep these two nuclei together. The kinetic energy depends on two parameters; mass of the nuclei and square of the nuclei's velocity. In classical sense, energy of the particle, which is required to overcome the barrier, must be greater than:

$$B = \frac{Z_1 Z_2 e^2}{R}, \tag{3.17}$$

where Z_1 and Z_2 are the atomic masses of the two nuclie, e is the charge of the electron,and R is the distance between these nuclie [1].

Although the kinetic energy must be larger than the Coulomb barrier in the classical sense, particles with less energy than the barrier can achieve the reaction as well due to the $quantum\ tunneling$ phenomena. The phenomena is based on the particle-wave duality theory. According to this theory, particle can behave like a wave to penetrate the classically forbidden barrier by tunneling.

There is also another barrier, which is called the $Q - value\ barrier$, to determine energy of the reaction. A typical reaction can be expressed as x + X –> y + Y, where x is the projectile, X is the target, and both y, and Y are the products. The $Q - value$ is difference between masses of the reactants and the products, and represented in energy units (usually MeV). It can be calculated in terms of either the Einstein's famous formula, $E = mc^2$, or kinetic energy of the particles (T). Moreover, sum of the Q-value and T_x should be greater than zero. It is necessary for a nuclear reaction to be accomplished. This relation can be written as;

$$Q = [m_{\mathrm{X}} + m_{\mathrm{x}} - (m_{\mathrm{Y}} + m_{\mathrm{y}})]c^2, \tag{3.18}$$

or,

$$Q = T_{\mathrm{Y}} + T_{\mathrm{y}} - (T_{\mathrm{X}} + T_{\mathrm{x}}). \tag{3.19}$$

Positive, or negative result of the $Q - value$ determines whether the reaction is endothermic or exothermic. The positive Q-value means there is an increase in kinetic energy for the final state, and this reaction is called **exothermic** (exoergic). In contrast, the negative Q-value represents an **endothermic** (endoergic) reaction [36].

CHAPTER 4

EXPERIMENTAL SET-UP AND METHODS

4.1 Target and Its Preparation

One of the most crucial points in the radioisotope production is selection of a proper target. It should have a high purity as much as possible in order to prevent occurrence probability of inevitable sub-reactions. Purity of the target is directly proportional to the enrichment rate. In the current study, the TiO_2 target is used with an enrichment of 96.9$\%$. Its sufficient properties, such as its considerably high purity, minimize detection of the other sub-reactions during the irradiation, and these properties make it a promising target for the ^{43}Sc production. Twenty-five different Ti targets (Figure 4.1) were prepared in suitable thicknesses and masses. Thickness should be sufficiently small for both to prevent the energy loss, and to achieve the irradiation with enough activity. Moreover, atomic mass of the ^{46}Ti radioisotope is 45.9526 g/mol, whereas the molar mass of TiO_2 is 77.9 g/mol.

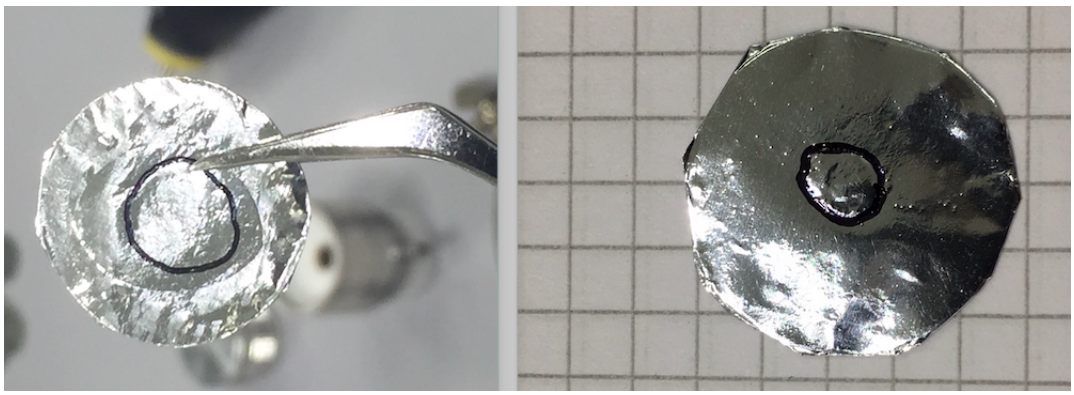

Figure 4.1: Ti target and the irradiation area

In the previous study, the enriched ^{43}Ca target was used in the form of $CaCO_3$ with an enrichment probability of 57.9%. In addition to ^{43}Ca, ^{44}Ca radioisotope was observed due to the low purity rate of the target. Hence, there were two different reactions to produce ^{43}Sc; $^{43}Ca(p,n)^{43}Sc$ and $^{44}Ca(p,2n)^{43}Sc$. The cross-sections of these two different reactions were separated carefully by irradiating $^{44}CaCO_3$ as well. It helped to get a distinctive result for the $^{44}Ca(p,2n)^{43}Sc$ reaction [37].

In the fixed frequency cyclotrons, energy degradation is required to perform irradiations at different energy levels. Likewise, the fixed energy of the Bern medical cyclotron needs to be degraded so that more accurate measurements for the ^{43}Sc cross-section can be obtained. Different numbers of aluminum foils with a thickness of 100 μm are used for the degradation (Figure 4.2). These aluminum foils are placed in front of the target before the irradiation to decrease energy of the bombarded particle. Al has a good thermal conductivity of 2.37 $W.cm^{-1}.C^{-1}$, which allows cooling of the target in a short period. Moreover, it has a high energy threshold of 31.86 MeV for the proton activation. Consequently, using Al foils decreases the possibility of impurities during the irradiation [1]. The procedure is simulated by SRIM Monte Carlo simulation to identify the stopping range of ions regarding the interactions of ions and atoms in matter. Determining variables, such as width of the Al foils, energy of protons, and total number of ions can be estimated through this simulation. Uncertainties in the thickness of Al foils are caused by the manufacturer, and they are given as $\pm 10\%$. This uncertainty is cross-checked by measuring thickness of the target with a millimetric measure. The exact measurement of the target area is essential not only for well-focused irradiations, but also for making reliable calculations. ImageJ, which is an open source image processing program, is used as a tool for measuring areas in every shape and in a precision of mm^2 (Figure 4.3). Measurements of lengths, angles, and standard deviations are also possible by ImageJ [38]. Since the mass of the titanium target is already known, the density in [g/cm2] is easily calculated by using the measured area.

Figure 4.2: Aluminum foils as the energy degrader

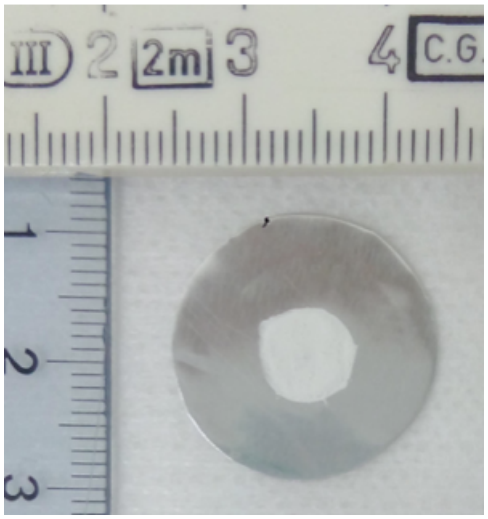

Figure 4.3: The Ti target and calculation of the irradiation area in the scale of mm^2

4.1.1 Irradiation and the Experimental Set-Up

Since the ^{43}Sc production emerges in Beam Transport Line (BTL), it is the most important part of the cyclotron. Apart from the BTL components, a target holder (Figure 4.4) is required to place the target properly, and keep it fixed during the irradiation. The holder includes a plastic cup, which isolates the grounded collimator, and a secondary electric blocking ring. Moreover, an extra plastic cup is mounted for fixing the target location. Before the irradiation process, the current and the voltage cables are connected to the holder, and then they are placed inside of the KF50 tube (Figure 4.6, and Figure 4.7).

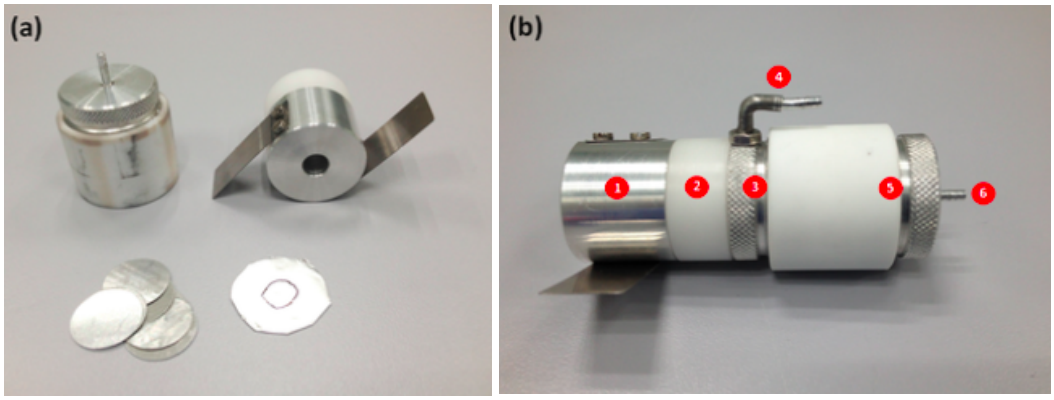

Figure 4.4: (a) Target holder with Al foils, and the Ti target, (b) Target holder and its components; (1) collimator of 6 mm (2) plastic cup, (3) secondary electron blocking ring, (4) voltage supplying pin, (5) cup of the target location, (6) current readout pin.

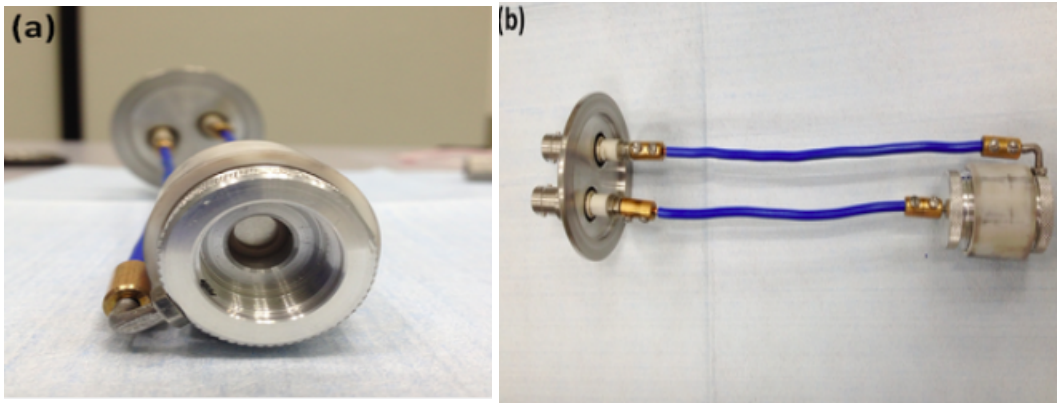

Figure 4.5: Front view (a), and side view (b) of the target holder, the collimator, and the plastic cup.

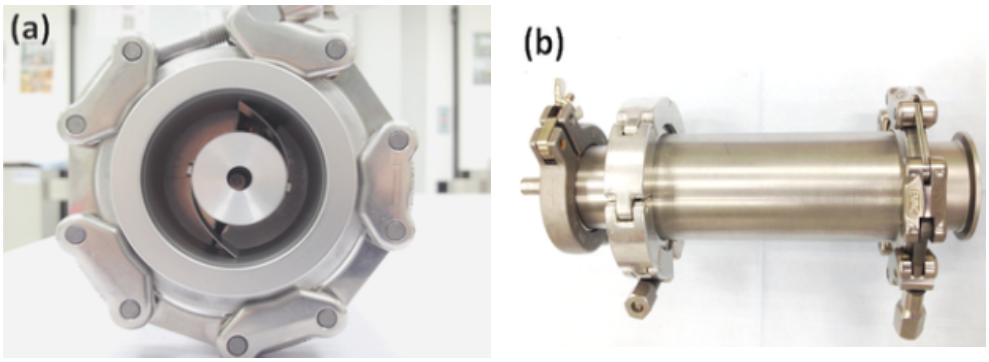

Figure 4.6: (a) The target holder placed inside of the KF50 tube, (b) side view of the KF50 tube

The proton beams should be aligned, and focused to the target in order to efficiently produce particles. Any possible loss in the secondary electrons, which would be

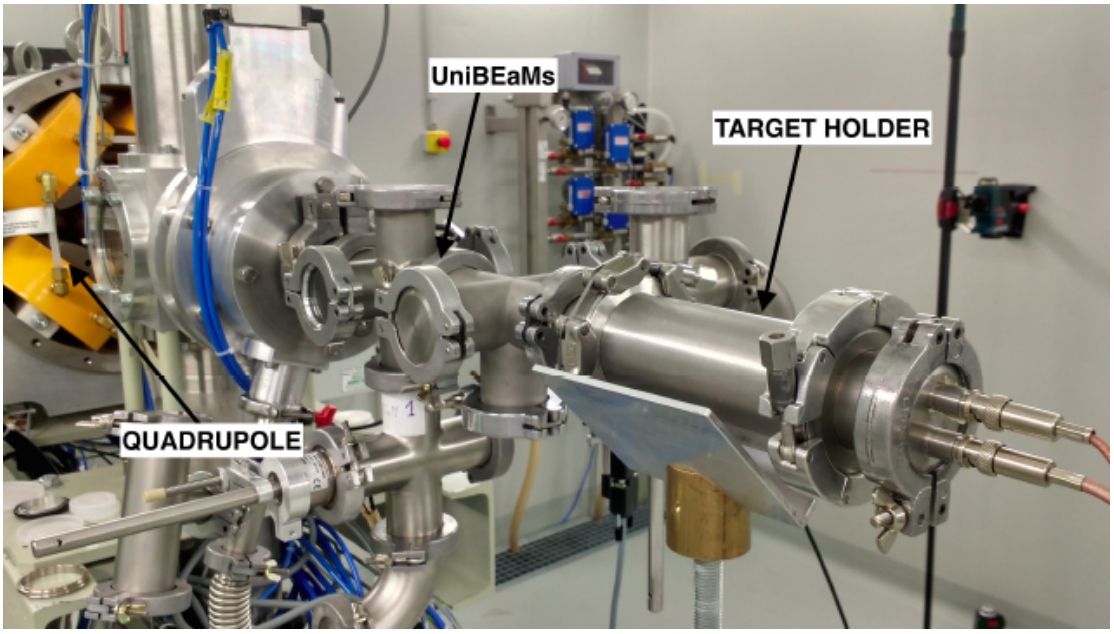

Figure 4.7: Quadrupole, KF50 tube installed in the BTL, and UniBEaMs

obtained during the irradiation, may cause some inevitable errors in the measurement of the current applied on the target. There is a repelling ring to minimize the effect of these errors by directing the electrons back to the point of origin [37].

The production is performed with a high transmission rate at different energy values, which are provided by the aluminum foils. A well-focused beam is also required for the highly transmitted productions. It ensures high efficiency, and reliability of the process. Two types of beam monitors, destructive and non-destructive, estimate accuracy of the beam monitoring. While the destructive one limits continues irradiations by interrupting the beam, the non-destructive beam monitors are developed and used for the hadron-therapy. They reveal ultra-high performance compared to the conventional methods, such as Faraday cups, by providing good quality images and making the control of the beam possible during the irradiation [39].

Irradiation area of the Ti target has a diameter of 6 mm. The beams should be focused within this specified area. Hence, the XY steering magnets are installed into BTL to adjust optical position of the beam line as centered as possible (Figure 4.8) [11]. Additionally, the cyclotron is equipped with two different beam viewers; one is placed at the exit port of the cyclotron, and the other one is placed in BTL. Generally, duration of the process is set between 2 to 5 minutes depending on the current value,

and there should be a waiting time before irradiating the same target again in order to minimize the possibility of observing sub-reactions during the activity measurement. The cyclotron is operated in the control room (Figure 4.10), and the current on the target is recorded with a digital electrometer, and the power is provided with a power supply (Figure 4.9).

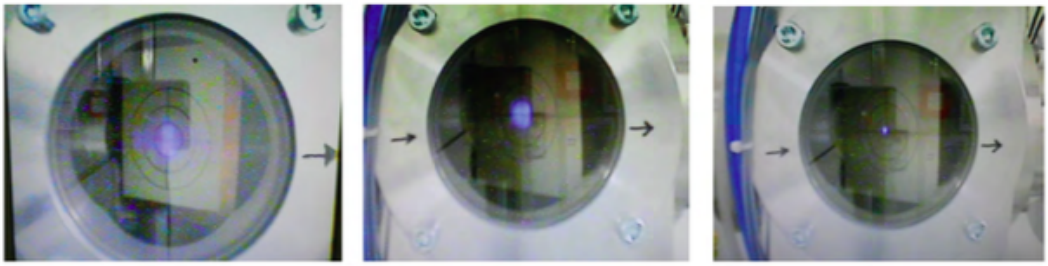

Figure 4.8: View of the beam after the first beam viewer and after the second beam viewer [11]

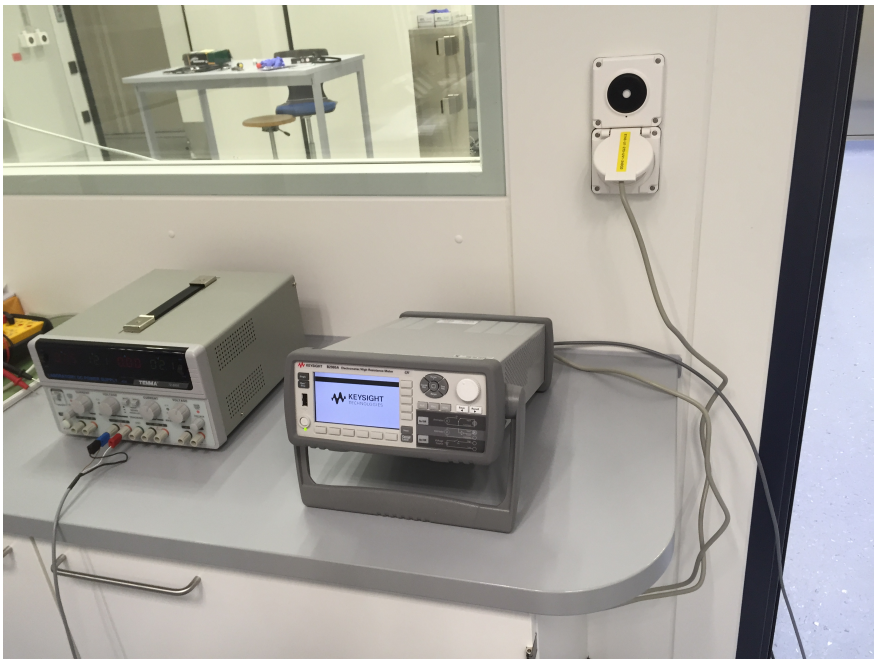

Figure 4.9: The power supply and the electrometer

Figure 4.10: The control room

4.2 The Bern Solid Target Station

The IBA Cyclone 18/9 Bern medical cyclotron has an extraction port, which is dedicated to the solid target station (STS). The NIRTA solid target station (IBA) was installed in the first part of 2016. I am involved in the irradiation tests performed with the natural titanium targets. During these irradiations, ^{48}V was obtained via $^{nat}Ti(p,x)^{48}V$ reaction. ^{48}V has a half-life of 16 d, a positron emission of 50%, and two high abundance gamma rays; one at 984 keV and the other one at 1312 keV. The production steps for the ^{43}Sc are repeated to obtain the ^{48}V radioisotope with desired cross-section values. Natural titanium has a molar mass of 47.96 g/mol, and a density of 4.506 g/cm^3. The coin target is prepared with a radius of 5 mm, a thickness of 0.075 mm, and a mass of 0.026 g (Figure 4.11).

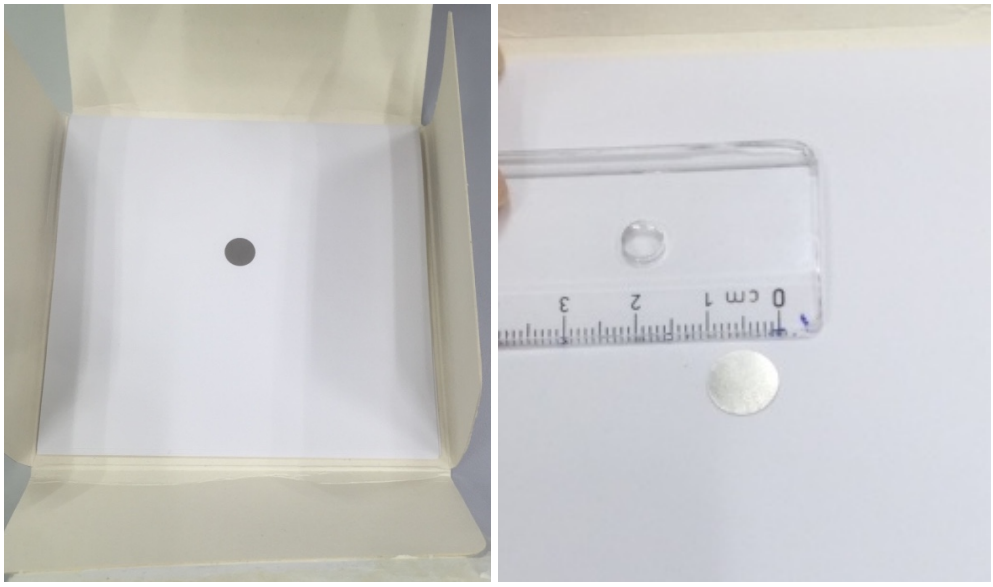

Figure 4.11: The natural Ti target (left) and representation of its size (right)

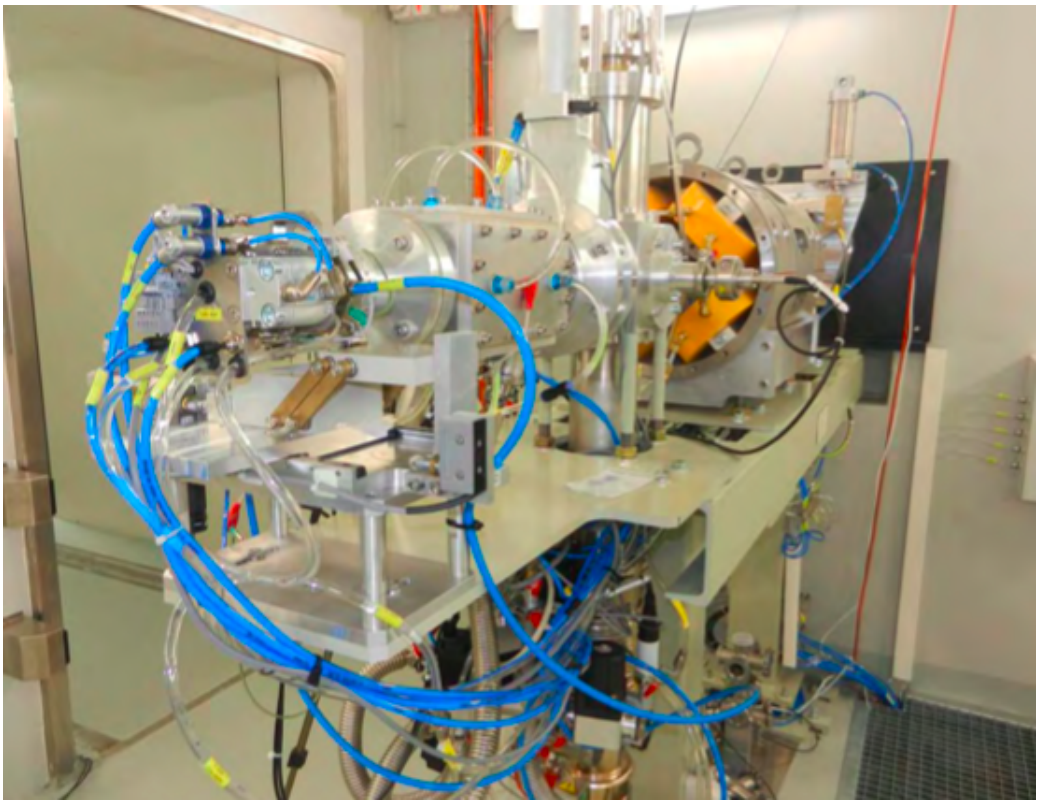

Figure 4.12: The BTL view of the solid target station [14]

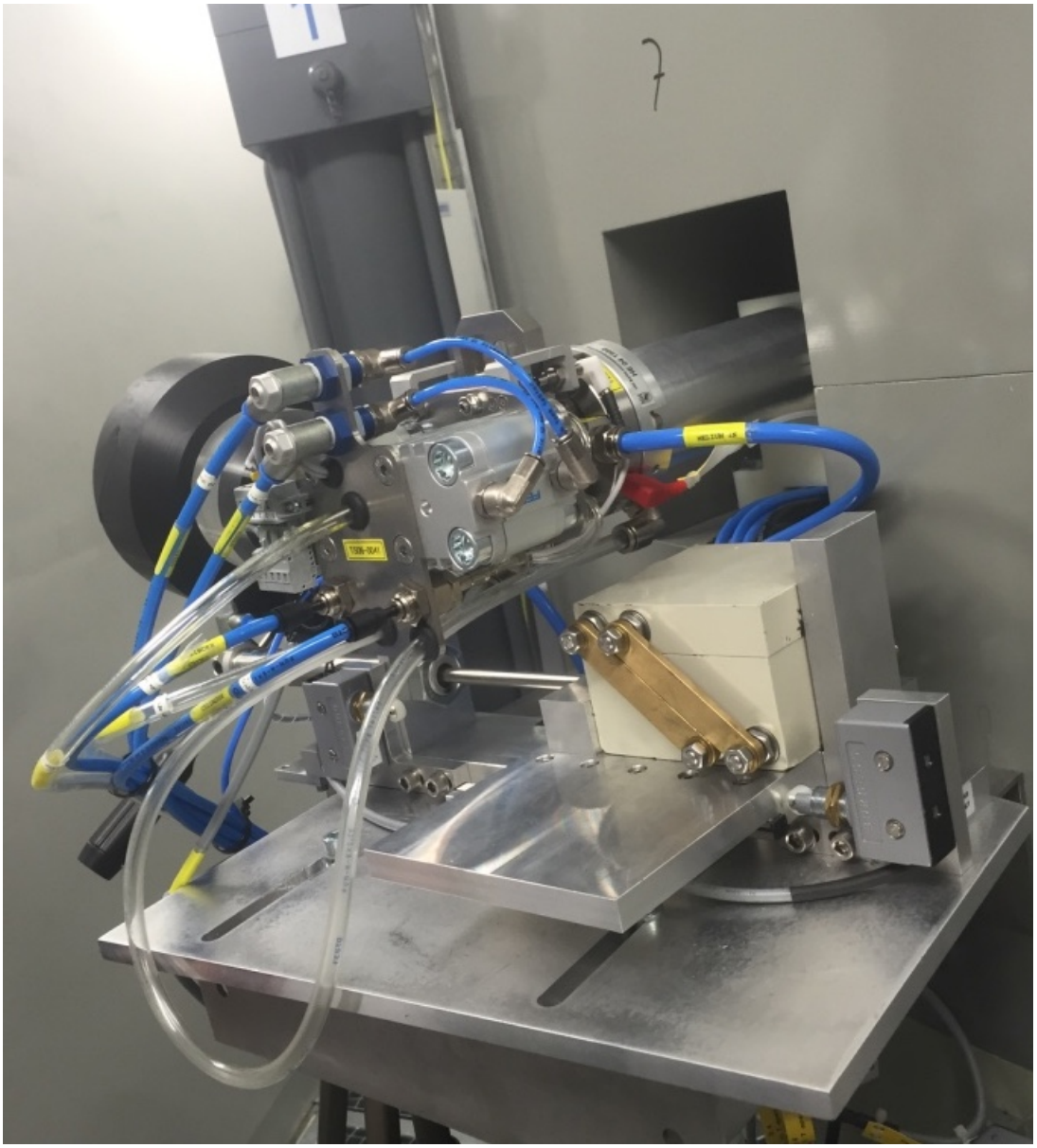

Figure 4.13: The cyclotron view of the solid target station [14]

In case of the solid target station, the highest radiation protection standards are provided. Since there is no requirement of opening the bunker doors of the cyclotron, irradiation time and radiation exposure dose decrease. It can be operated both on BTL and on the cyclotron (Figure 4.12 and Figure 4.13). A target disk is mounted in the station in order to keep the target stationary. The target should be placed manually into the cavity of the disk (Figure 4.14). The diameter of the disk is 23.95 mm and its thickness is 1.90 mm, whereas diameter of the cavity is 12 mm. Moreover, the station is equipped with an aluminum window foil of 500 μm thickness, which degrades the

cyclotron energy from 18 MeV to 14.9 MeV [14]. The aluminum foil has enough durability under the high radiation doses. Additionally, the thickness of the target is smaller compared to other type of targets, and it decreases path length of the beam.

On the other hand, cooling of the target is important to avoid decomposition of the materials and to make irradiations possible at a higher power (up to 500 W). Back side of the target (Figure 4.15 (right)) is cooled by water, while its front side (Figure 4.15 (left)) is cooled by helium. The reason of using helium as a cooling material for the front side is to prevent unwanted interactions of water and protons. Magnets on the disk (Figure 4.20) lead to a water leak during the irradiation, which might cause corrosions on metal parts and damage the electronic components. Hence, a new disk was designed by the Bern workshop and the magnets were placed inside of the disk to avoid these consequences.

As the next step, the shielded box should be positioned below the target station in an open state (Figure 4.16) so that the highly radioactive target can fall down into this box after the irradiation is completed (Figure 4.17). After introducing the disk, locking it to the target station, checking the helium and water cooling status, and the beam request, the target can be irradiated for 2-5 minutes as usual. Before unloading the target disk, the cooling water should be purged and the back side of the disk should be dried for 1-2 minutes. These steps can be monitored by the camera that is installed for the visual operation of the process (Figure 4.18) [14].

Figure 4.14: Open (left), an closed (right) representation of the target holder

Figure 4.15: Front side (left), and back side of the the target holder and the magnets on it (right)

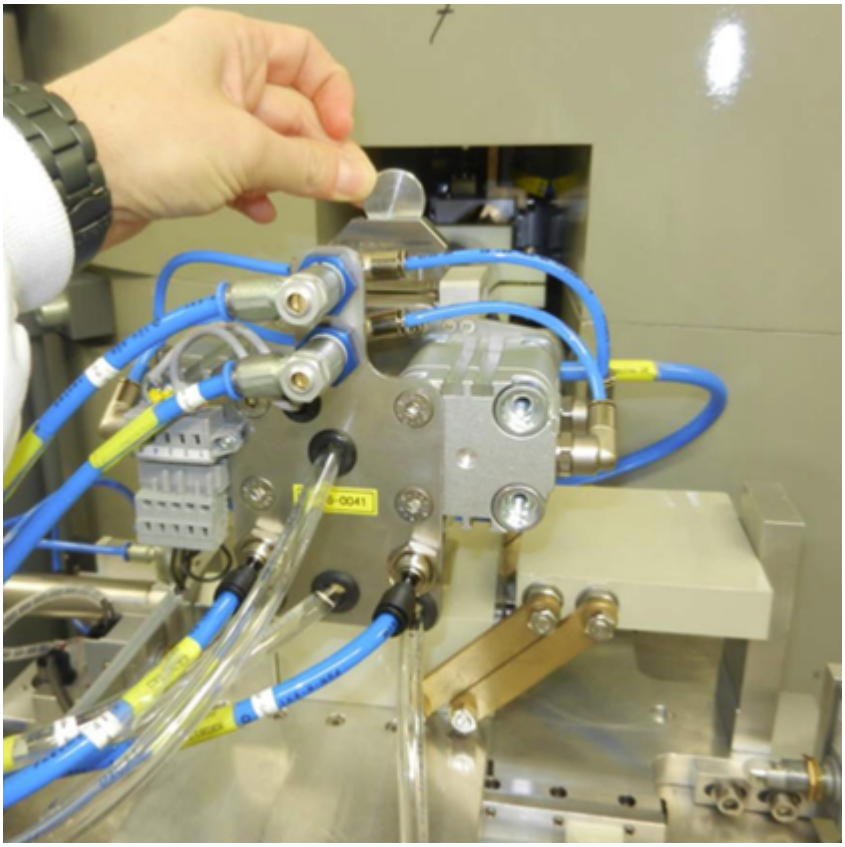

Figure 4.16: The shielded box below the solid target station and the general view of the STS [14]

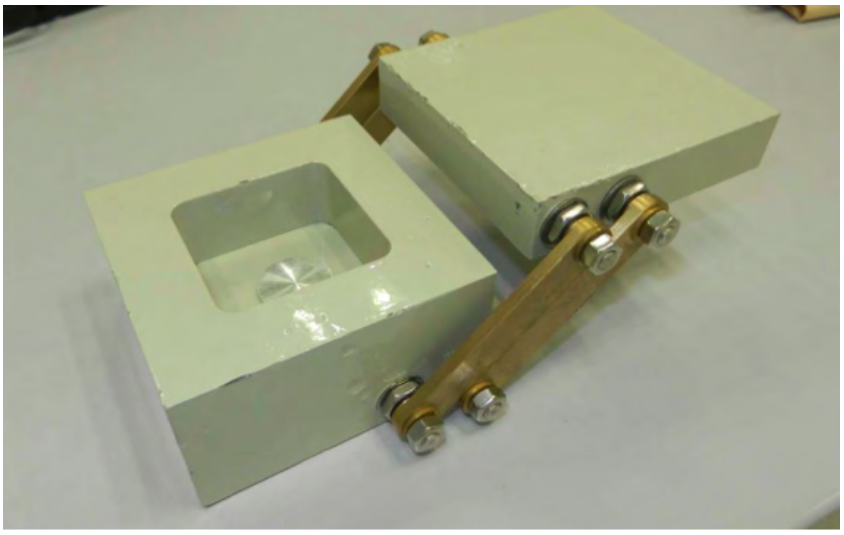

Figure 4.17: The shielded box [14]

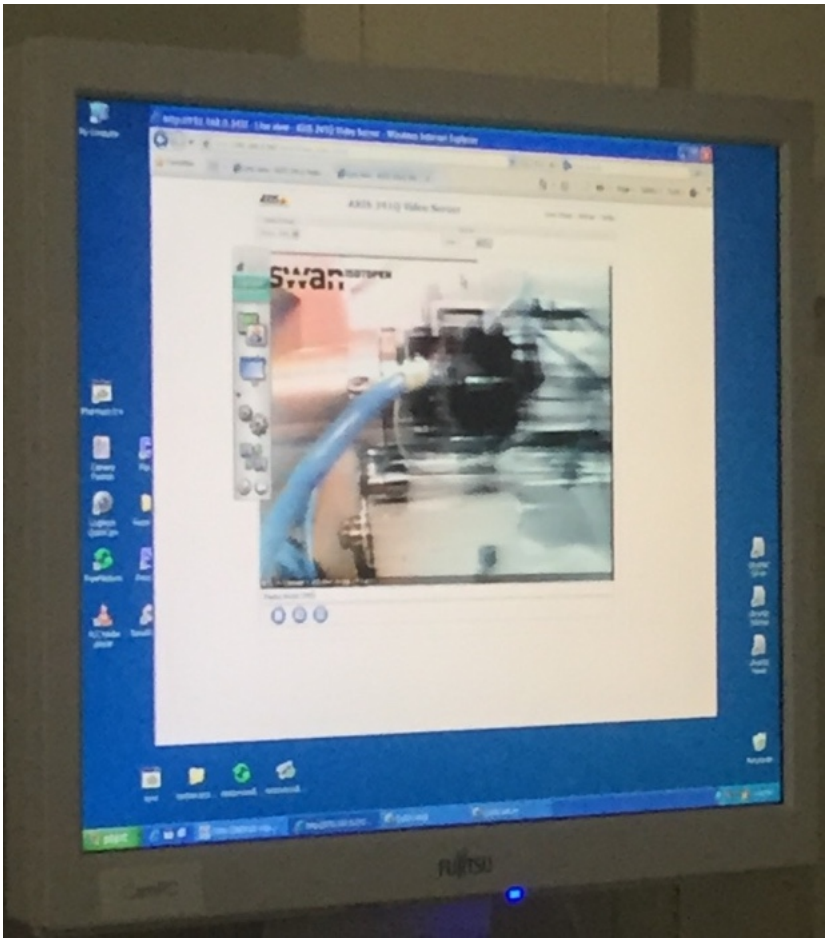

Figure 4.18: Monitoring of the production steps [14]

4.3 Germanium Detector and Radioactivity Measurement

The radioactive decay is a statistical process and can be predicted by assuming that individual nuclear decays are purely random events. If there are N radionuclides at some time t, then the number ΔN, which would decay in any given time interval Δt, is proportional to N:

$$\Delta N = -\lambda N \Delta t \tag{4.1}$$

which leads to the exponential decay formula:

$$N = N_{\circ} e^{-\lambda t} \tag{4.2}$$

where λ is the radioactive decay constant.

In this experiment, the activity rate presented in Eqn. 4.1 is measured with the High Purity Germanium Detector (HPGe). It is a device to observe interactions of matter with gamma rays. These interactions can be named as the photoelectric effect, the Compton scattering, and the pair production. Formations of the possible interactions and their schematic representations in the gamma ray spectrum can be seen in Figure 4.19 and Figure 4.20. As a result of these interactions, gamma particles give their energies to electrons or to positrons, and produce ionized atoms as the secondary particles. Signals obtained from these ions allow drawing the basic characteristics of the radioactive materials regarding their peak location, peak area, energy and efficiency values, and radioactivity quantification. The detector efficiency is shown by ϵ, and it refers to the relation between the number of counts before and after the irradiation. The high efficiency allows to measure the activity more precisely. Another important factor that affect the gamma ray spectroscopy is the resolution of the detector. Each energy peak should be observed clearly in order to make the energy levels distinguishable, generally in the order of keV[40]. The detection of the many ions simultaneously induces a dead-time problem, which can be defined as the intersection of two different events in a defined time interval. It is another important factor for the activity measurement, and the events occurred during this intersection period cannot be observed. Hence, the lost information cause the approximate measurements. There are some correction and estimation models for the dead-time in order to minimize its effect, and to get the most accurate values. Although it can be acceptable up to 10%, the lower value of the dead-time means the more efficient results of the activity [41].

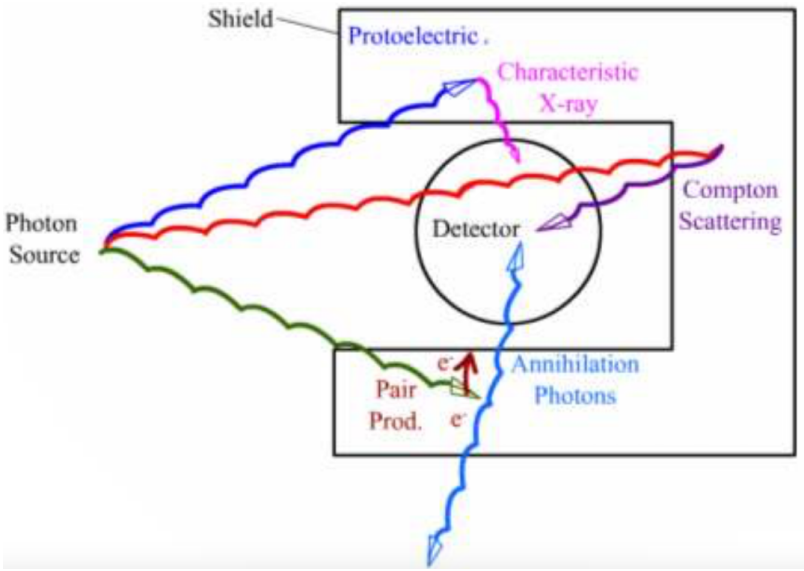

Figure 4.19: The possible interactions of gamma rays with matter and their detections with the HPGe detector [8]

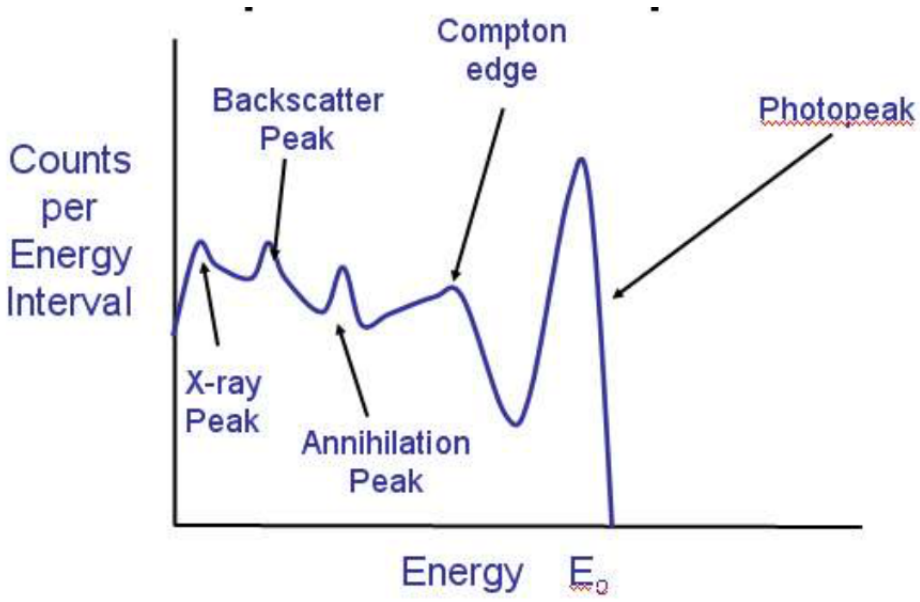

Figure 4.20: A symbolic representation of the possible interactions in a gamma ray spectrum [8]

On the other hand, the detector calibration must be taken into account carefully in order to prevent undesired results of the activity measurement. The calibration includes energy, resolution, and efficiency of the detector. Firstly, the energy calibration is required to prevent consequences of possible instabilities of the electronic devices placed inside of the detector. Accuracy of the different energy scales, that are used to

determine the energy regions at different intervals, are considered as well. Secondly, an accurate complementation of the peak width and the automatic peak analysis result in a good energy resolution. This procedure is known as the Full Width at Half Maximum (FWHM), and it makes the resolution calibration essential to obtain a good match between the best peak line and the counts of the spectrometer. Finally, the efficiency calibration has an important influence on the constant activity outcomes. The calibration samples are prepared in order to replace the real samples. They should have the same physical and chemical properties with the original samples. Also, their activities should be known exactly [42]. There are two high purity germanium detectors in Inselspital, and they are shown in Figure 4.21. The principle of the analysis is based on the Genie 2000 gamma ray spectrum analysis software.

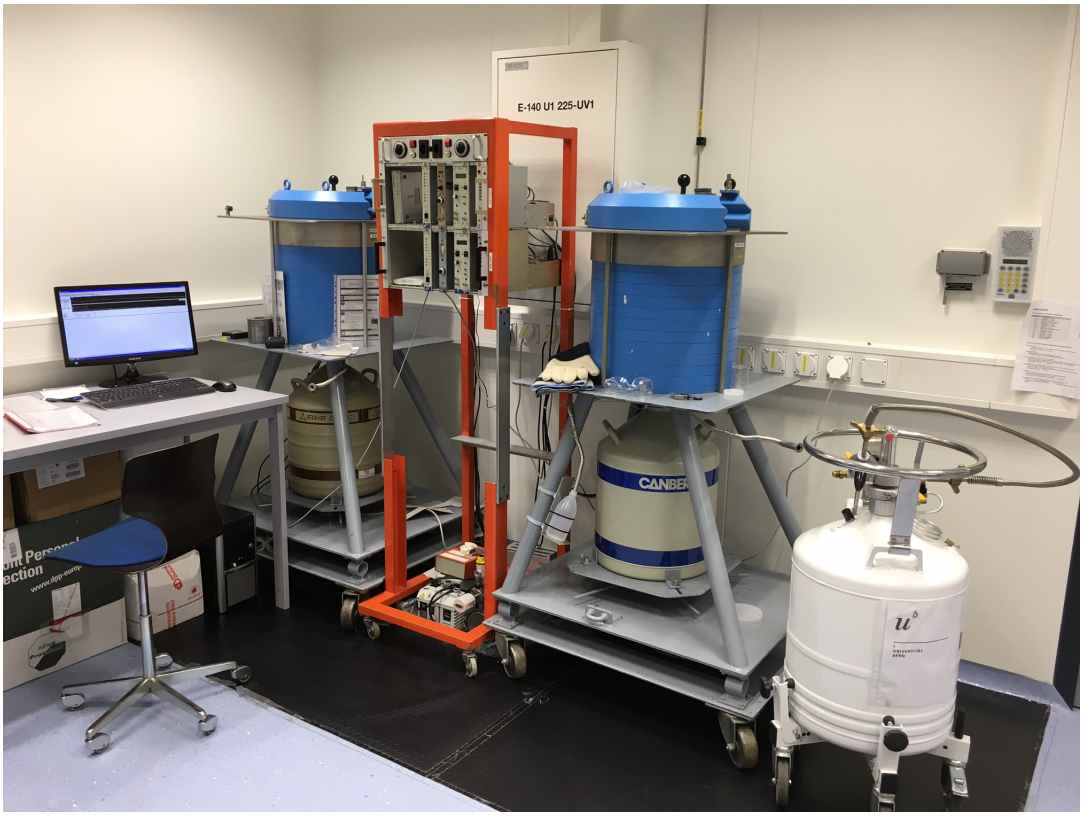

Figure 4.21: Two germanium detectors in the Bern medical cyclotron laboratory

As it was mentioned above, the irradiation results are analyzed by the HPGe detector. Before placing the target inside of the detector, it must be cooled to minimize the activity contributions of the other radionuclides, which are produced as a result of the undesired reactions. The time required for this period is called the cooling time,

and represented as t_c. The duration of the cooling must be long enough to cover the half-life of the activated particles. Elimination of the unnecessary decays by cooling is also important for the low dead-time.

After the cooling step, irradiated target becomes ready to be placed inside of the germanium detector. Generally, the measurement takes between 15 to 20 minutes depending on the dead time, and on how properly the excited states are observed. The primary excited state of ^{43}Sc in the gamma ray spectrum of enriched-titanium (TiO_2), are observed at 372.9 keV. There is also another peak at 511 keV, which represents the electron-positron annihilation. After the measurement is completed, the gamma ray spectrum and the detailed analysis report including the required background subtractions, are exported. This report gives the net peak area of the 373 keV line with the net area uncertainty, the peak efficiency, and the efficiency uncertainty. The net peak area value is used to calculate the cross-section of the radioisotope as in Eqn. 4.5. Apart from the data obtained by the detector, there are also other parameters that belong to the ^{43}Sc, namely the decay probability of 22.5%, and the half-life of 3.89 hours. Additionally, the detector efficiency of 0.0597 for ^{43}Sc, time of the measurement, and time of the cooling are also mandatory to calculate the activity. The SI unit for the activity is Becquerel (Bq).

The unique excited state of ^{43}Sc at 372.9 keV allows measurement of the radioactivity without applying extra steps to distinguish possible sub-reactions. On the other hand, elimination for the undesired contributions of the secondary reactions were required in the previous study. Based on the impure targets, i.e. $^{43}CaCO_3$ and $^{44}CaCO_3$, many energy lines were detected which referred to ^{43}Sc, ^{44}Sc, ^{27}Mg, ^{52}V and the positron-electron annihilation. The isotope composition of these two targets can be seen from Table 4.1 [37].

Table4.1: The isotopic compositions of $^{43}CaCO_3$ and $^{44}CaCO_3$ targets

Isotope	40	42	43	44	46	48
enrichment (%)	28.5	1.05	57.9±1.8	12.36	<0.003	0.19
enrichment (%)	2.89	0.06	0.03	97.00±0.2	<0.002	0.02

4.4 The Cross-Section Measurements

The production cross-section is defined as an interaction probability of particles in a given transverse area [43]. For this more specific case, it can be taken as the rate of the formation of a nucleus or the rate of the separation of a nucleus into sub-particles. The unit of the cross-section can be taken as cm^2, but also as barn (b), which equals to 10^{-24} cm^2. There are both theoretical calculations and literature data for the cross-section of the each reaction. The TENDL-2015 data base (TALYS-base evaluation nuclear data library) [44] can be interpreted as the source of the theoretical data, while the EXFOR (Experimental Nuclear Reaction Data) database provides the experimentally obtained values [45]. However, the measured values are not always compatible with these data, especially in the light nuclei case. Hence, having several measurements becomes necessary to check the accuracy of the results. All required variables for the cross-section calculation are acquired by the activity measurement. The calculation is obtained by exploiting a group of formulas such as some decay properties of the corresponding radioisotopes, features of the targets as well as the results of the gamma ray spectroscopy. Irradiation area a_i (cm^2) is defined as:

$$a_i = \pi r^2 \tag{4.3}$$

where r (cm) is the radius of the irradiated area.

The projectile flux $(protons/s.cm^2)$ is calculated using the current on the target I (C/s), the target area, and the elementary charge e (C) with the formula:

$$\phi = \frac{I}{a_i e} \tag{4.4}$$

The total number of target atoms per unit area $(atoms/cm^2)$ is obtained from:

$$N = \frac{m_T N_A f}{M a_T}, \tag{4.5}$$

where m_T is the target mass (g), N_A is the Avogadro number (mol^{-1}), M (g/mol) is the molar mass of the target molecule, a_T (cm^2) is the target area, which is obtained

by ImageJ software, and f is the fraction of the target atom in the target molecule and is calculated as:

$$f = \frac{M_A}{M} I_A, \tag{4.6}$$

where M_A (g/mol) is the molar mass of the target atom and I_A is the isotopic enrichment of the target.

By the combination of these formulas, the calculated activity A_{cal} (s^{-1}), can be formulated as:

$$A_{cal} = \phi\sigma N(1 - e^{-\lambda t_i}). \tag{4.7}$$

By inserting Eqn. 4.4 into Eqn. 4.7,

$$A_{cal} = \frac{I\sigma N(1 - e^{-\lambda t_i})}{ea_i}, \tag{4.8}$$

where N ($atoms/cm^2$)is the total number of the target atoms per unit area, and t_i (s) is the time of irradiation, while σ (mm^2) is the cross section value of the reaction. By rewriting Eqn. 4.8, the cross section formula can be obtained as:

$$\sigma = \frac{A_{cal} e a_i}{IN(1 - e^{-\lambda t_i})}, \tag{4.9}$$

In order to compare the measured activity with the calculated value, A_{mes} (s^{-1}) can be extracted from the values obtained by the gamma ray spectroscopy following the formula,

$$A_{mes} = \frac{net\ peak\ area}{\epsilon P \tau e^{-\lambda t_c}(1 - e^{-\lambda t_m})}, \tag{4.10}$$

where ϵ is the efficiency of the germanium detector and defines the number of pulses in a given number of gamma rays, t_m (s) is the required time to complete the measurement of the gamma ray spectroscopy, and t_c (s) is the required cooling time after the

irradiation. Moreover, τ, inverse decay constant, equals $1/\lambda$ (s^{-1}) where λ is the decay constant. The net peak area is obtained from the gamma ray spectroscopy of the target at 373 keV line, given that P is the decay probability of the target at the same energy line with the corresponding value of 22.5% for ^{43}Sc. The measured activity can be used to cross-check the accuracy of the cross-section calculation by putting A_{mes} instead of A_{cal} in Eq.4.8.

The measured activity are ensured by the calibration of the HPeG detector as well. The time elapsed t_{elap} from the beginning, the half-life of the radioactive sample, its initial $A(_i)$ and final $A(_f)$ activities are enough to check the accuracy of the detector following:

$$A_f = A_i e^{-\lambda t_{elap}}, \tag{4.11}$$

and by taking natural logarithm of both sides, previous equation can be rewritten as:

$$t_{elap} = -\frac{t_{1/2}}{ln2} ln \frac{A_f}{A_i}. \tag{4.12}$$

CHAPTER 5

RESULTS

In this chapter, some numeric factors such as the energy degradation and the cooling time, that shapes the cross-section results, are presented. The activity measurements, the gamma ray spectroscopies obtained by the HPGe detector, and the detector calibration results are represented. Moreover, the measured cross-sections are discussed by comparing them with the EXFOR and the TENDL database to check the accuracy of these results. Possible reasons of some systematic errors and the possible solutions for the improvements are mentioned as well. Finally, the measurements for the ^{48}V radioisotope are shown, and the results are compared with the theoretical values.

5.1 The Energy Degradation and the Cooling Time

Several titanium targets are irradiated at different energies to determine the most precise measurements. As an essential step, the energy degradation with the corresponding uncertainties is performed by using the SRIM Monte Carlo simulation. The energy values versus the foil thicknesses graph including their uncertainties can be found in Figure 5.1, whereas the table of the transmission outcomes regarding the different Al thicknesses is represented in Table 1 (Appendix A). The maximum thickness of Al foils to be used for the degradation is 1800 μm, and above this thickness, it is not possible to observe a proton beam on the target.

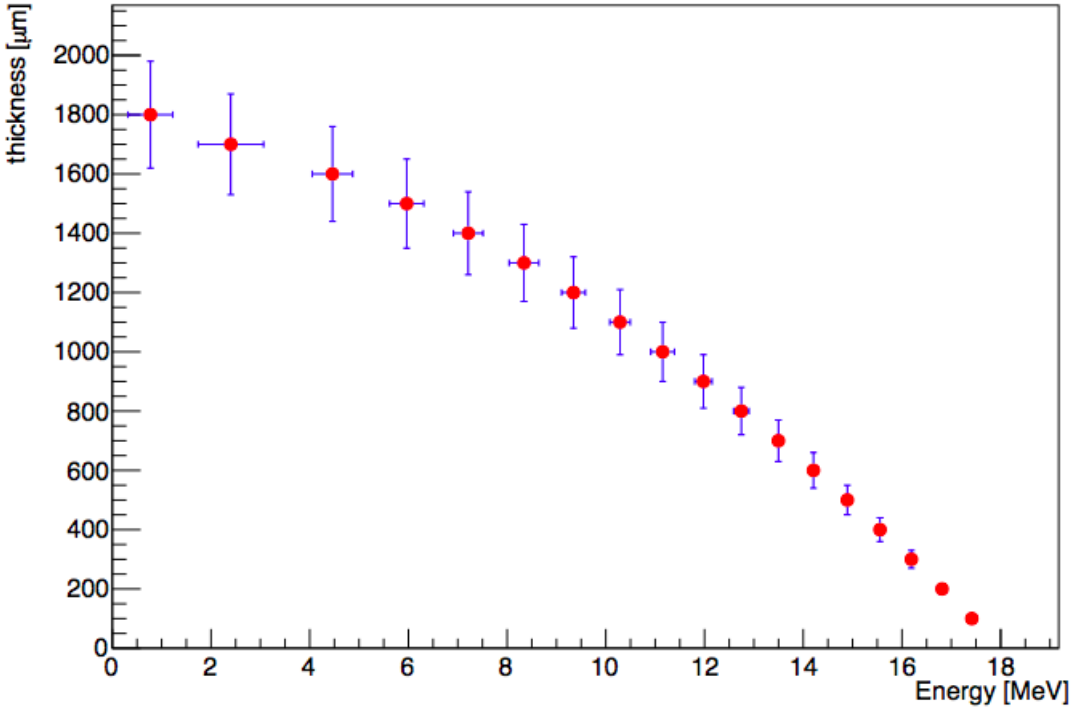

Figure 5.1: Energy degradation values at different Al thicknesses simulated by SRIM

The cooling time after the irradiation is another factor that shapes the results, since it directly affects the dead time. The dead time can be observed during the measurement, and it decreases as the cooling time increases. The relation between the dead time and the cooling time is illustrated in Figure 5.2, and the data are available in Table.2 (Appendix A).

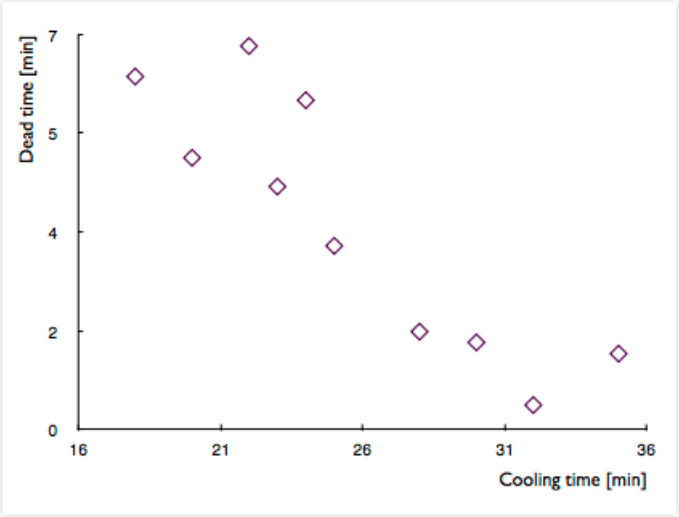

Figure 5.2: Relation between the dead time and the cooling time

5.2 The Activity Measurement and the Gamma Ray Spectroscopy

Activities for the corresponding productions are measured by using the outcomes of the HPGe detector. During the measurement, peaks of the different gamma lines are observed as well as the dead time to have a precise result. These peaks are analyzed regarding their location, their energy efficiency, and other background and correction properties. These analyses are exported as a report and can be seen in detail from Figure.1 (Appendix A). The report for the present measurement includes the net peak area at two different gamma ray energy values. ^{43}Sc has a unique gamma emission line at the energy of 373 keV, and the TiO_2 target is enriched at a rate of 96.9%, which is high enough to minimize the occurrence of any undesired emission. Hence, the peak observed at 373 keV (Figure 5.3) is referred to the ^{43}Sc radioisotope, and the area under this peak is measured as the net peak area of the ^{43}Sc radioisotope to measure its activity. As expected, another peak for the gamma ray produced as a result of the positron-electron annihilation (e^+e^-) is appeared at the energy of 511 keV in the spectrum. In addition to these specific lines, other small peaks represent the results of possible sub-reactions regarding the impurities in the Al foils and in the highly enriched target. A detailed view of the ^{43}Sc peak, and the area of this peak are schemed in the Figure 5.4.

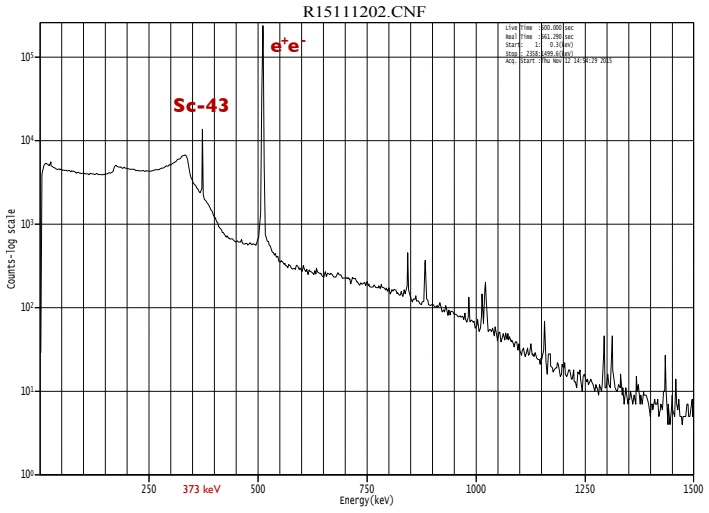

Figure 5.3: Gamma-ray spectrum for the $^{46}Ti(p,\alpha)^{43}Sc$ reaction at 14.9 MeV

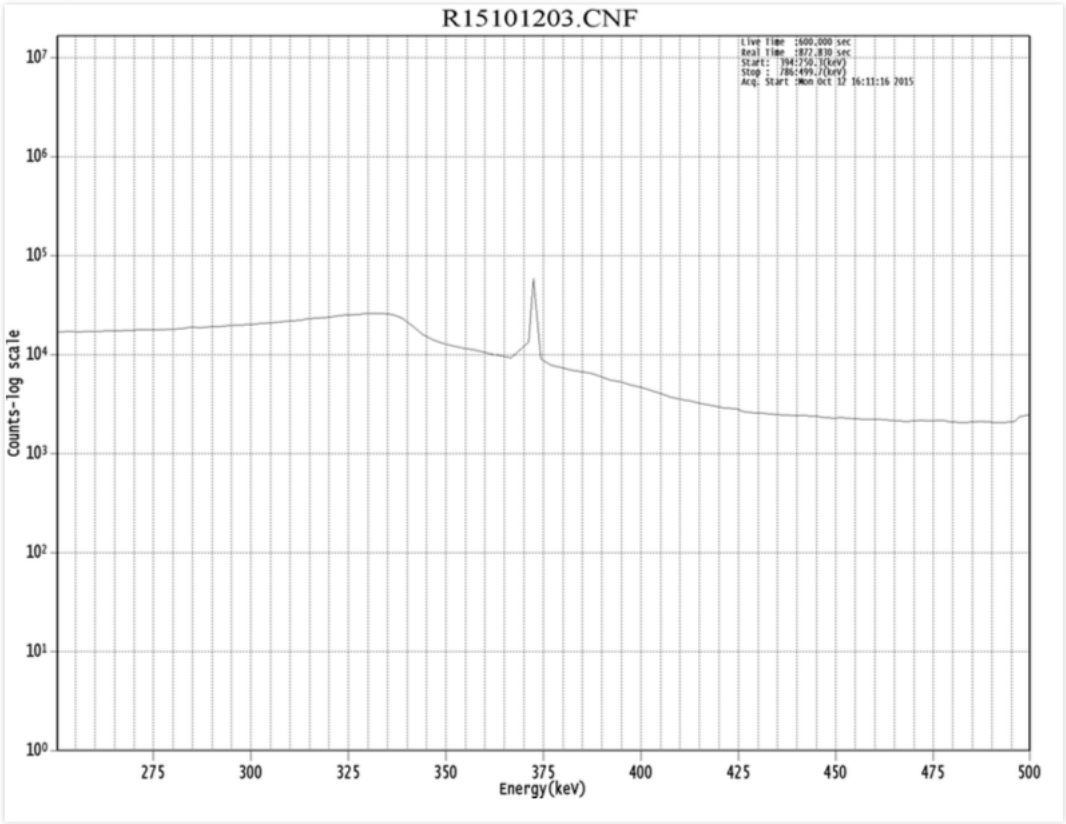

Figure 5.4: The unique gamma ray emission peak of the ^{43}Sc radioisotope at 14.9 MeV

During the first part of this study, unexpected activity results were observed due to a calibration issue. Hence, the process was repeated by using both old and newly prepared Ti targets after the detector calibration was improved. For the further measurements, the calibrated samples, namely ^{133}Ba with the activity of 37 kBq and $multi - gamma$ with the activity of 30 kBq are used to ensure the results. Since their gamma ray emission rates are high, there may occur some overlapped counts. In order to eliminate this possibility, a plastic spacer with a height of 78 mm is placed between the sample and the surface of the detector before the measurement. Some specific information for the calibration samples are listed in the Table 5.1.

5.3 The Cross-Section Results for the ^{43}Sc Radioisotope

After obtaining all required variables, the cross-section values are calculated by using the equation 4.9. The error on the mass and on the HPGe detector are taken into

Table5.1: Properties of the calibration samples

	^{133}Ba	multi-gamma
activity (kBq):	37	30
calibration date:	21.06.2001	25.11.2013
elapsed time (days):	5619	1079
time of measurement (s):	450	500
distance from the surface of the detector (mm):	78	78

account in order to determine their influences on the cross-section. The results of this study are compared to the values of the EXFOR and the TENDL database. Only one previous study, which was performed by Levkovskij in 1991 for the $^{46}Ti(p,\alpha)^{43}Sc$ reaction has been found in EXFOR. The cross-section of the corresponding reaction as a function of the cyclotron energy is presented with three different distributions in Figure 5.5. The black circle marker represents the theoretical data (TENDL-2015), while the blue circle (Levkovskij), and red star markers (the present study) compare the experimental results. Although the theoretical simulations and the experimental cross-sections of Levkovskij reach higher proton energies, the results for the present study can be obtained only up to 18 MeV proton beam energy due to the maximum energy limit of the Bern cyclotron. The measurements for the present study agree well with the TENDL-2015 database up to 13 MeV. However, the theoretical curve underestimates the experimental observations by 10 to 15 mb after 13 MeV. Whereas two experimental measurements differ up to 14 MeV, they yield the similar cross-sections for the higher energies. Although the maximum cross-section value for TENDL is observed at $31.42 \pm 1.6494\ mb$ with the energy of 13.5 MeV, the maximum production yield of ^{43}Sc that matches with the TENDL data is $25.37 \pm 1.234\ mb$ at the energy of $12.75 \pm 0.15\ MeV$. It can be obviously seen that the cross-section peaks, which belong to three different ^{43}Sc measurements, are between the energy values of 15 MeV to 17 MeV. All data used for calculation of the cross-section are listed in Table.3 (Appendix A). Moreover, a comparison between the results of the current study, and the EXFOR and the TENDL database values are presented in Table.4 (Appendix A).

5.4 The Systematic Uncertainties

The discrepancy on the graph can be explained by the following factors; current on the target, efficiency of the detector, or time required for irradiation, cooling, and measurement. During the irradiation, current on the target were observed in the $65\ nA - 145\ nA$ range, where the maximum current of the Bern cyclotron is 150 μA with a high transmission efficiency. The most suitable current and the energy combination can decrease differences between TENDL and our measurement. In addition, the error on the detector, which differs between 0.0100% and 0.0550% in this case, has an impact on the cross-section errors. The more accurate results can be achieved by improving the detector efficiency with the help of the regular calibration corrections. Moreover, the time for irradiation and cooling are important to perform proper bombardments, and to reduce the dead-time, as well as possibility of the undesired sub-reaction measurements. Duration of the activity measurement is also important to observe the gamma ray peaks effectively. Hence, the time for these processes can be optimized in order to decrease the discrepancies in the results. Another factor that effects the result can be uncertainties on the target mass. Precise measurements of the mass can increase accuracy of the cross-section values.

On the other hand, the titanium target offers a good agreement with the TENDL and the EXFOR data compared to the distribution for the previous study, which was performed by irradiation of the enriched calcium target [37]. However, future measurements should be performed in order to ensure the most desirable and accurate cross-sections for the ^{43}Sc radioisotope. Thankfully, the Bern cyclotron provides promising facilities with its new solid target station to perform future irradiations and consequently, to determine the best combinations for the ^{43}Sc production.

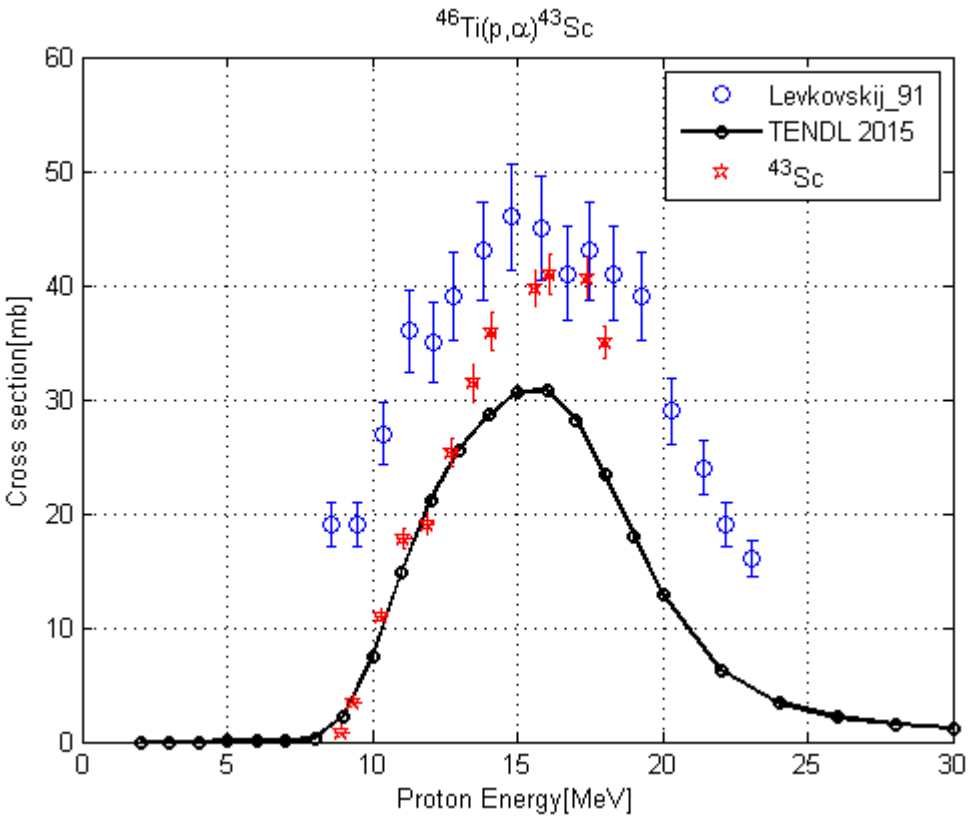

Figure 5.5: Cross-section distribution of $^{46}Ti(p,\alpha)^{43}Sc$ reaction compared with TENDL-2015 and EXFOR database

5.5 The Measurements for the ^{48}V Radioisotope

For the production of the ^{48}V radioisotope, two irradiations were performed through $^{nat}Ti(p,x)^{48}V$ by using the solid target station. Methods for the cross-section measurement described in section 4.2 were applied, and the results are presented in Figure 5.7. The ^{48}V radioisotope has two gamma emission line at 983 keV, and 1312 keV respectively. Since the target (^{nat}Ti) is natural, the undesired peaks are very few, and negligible. There is also one more peak due to the positron-electron annihilation. All these peaks can be observed in Figure 5.6.

The recommended values for the cross-section are provided by IAEA report [46], and figured in Figure 5.7 with the red curve. For the experimental results, there are two different points regarding their gamma ray energies. One result was obtained at the energy of 983 keV, whereas the other one was pointed at the energy of 1312 keV.

Both results show good agreement with the recommended data, and prove accuracy of the measurement process. A report for the gamma ray spectroscopy can be seen in Figure.2 (Appendix A).

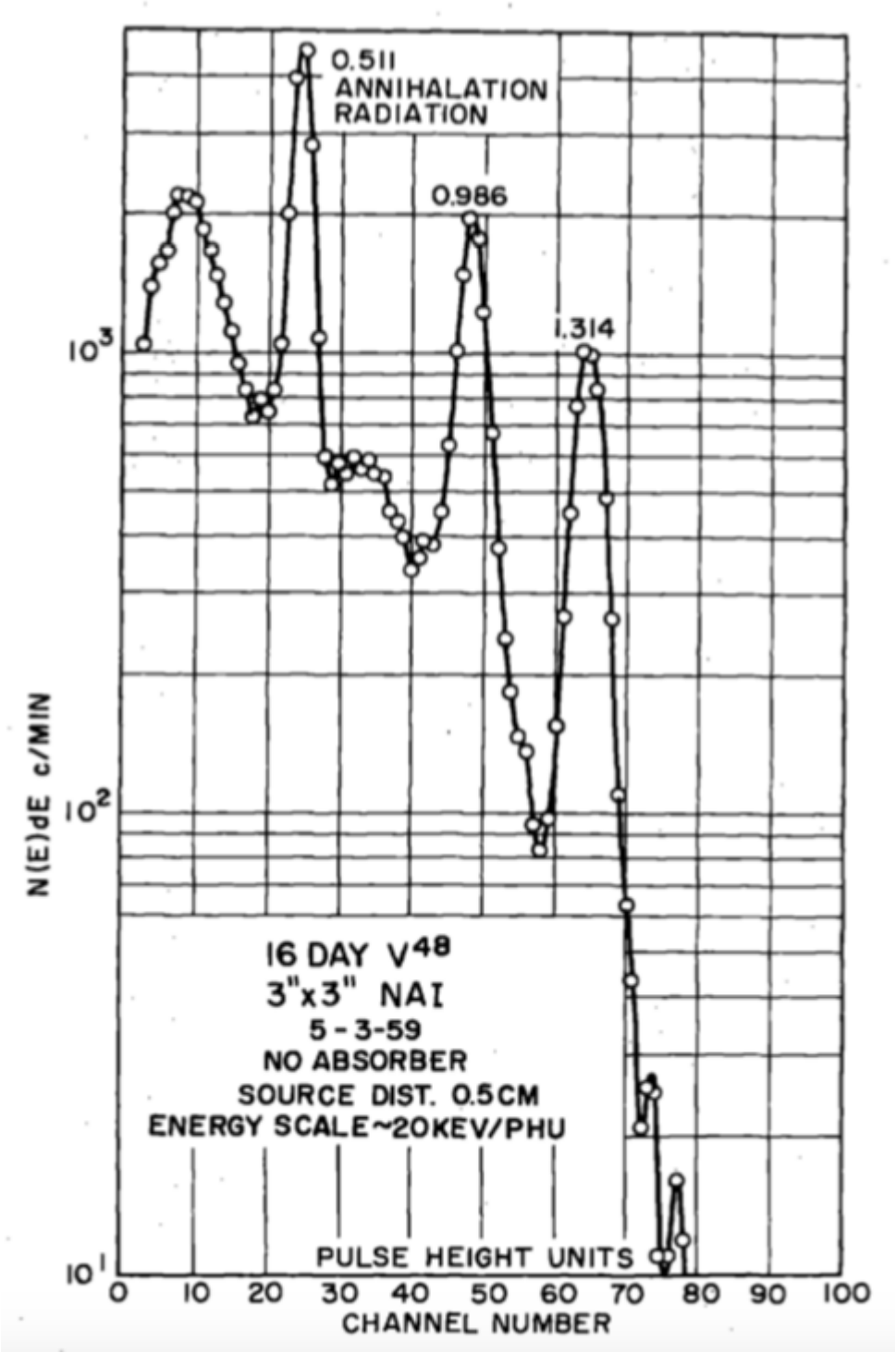

Figure 5.6: Gamma-ray spectrum of ^{48}V [15].

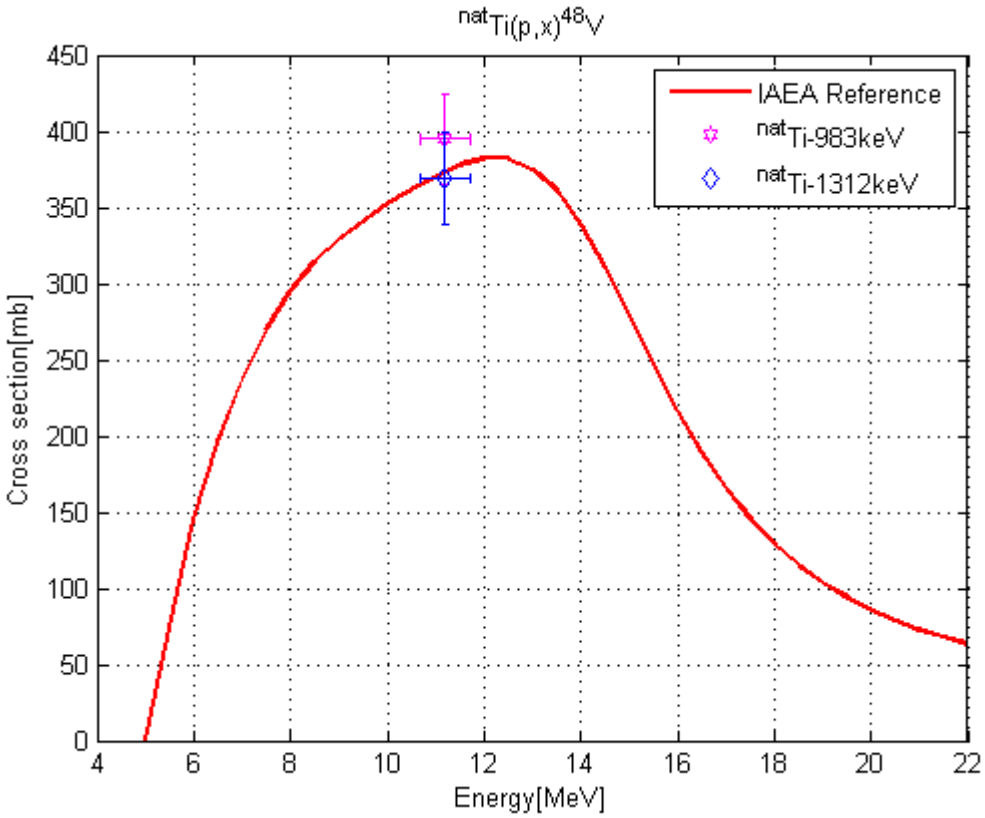

Figure 5.7: Cross-section distribution of $^{nat}Ti(p,x)^{48}V$ reaction compared with the recommended cross-section values of IAEA

CHAPTER 6

CONCLUSION

Among many advancements, PET is accepted as an outstanding technique providing state-of-the-art performance in the medical diagnosis. The aim of the present thesis is to determine the most favorable conditions to produce a novel radioisotope, namely ^{43}Sc, in the Bern medical cyclotron laboratory. The cyclotron laboratory has been constructed in order to gather radioisotope production, and it provides a multidisciplinary research environment. It has a fixed beam energy of 18 MeV, and is equipped with a beam transport line (BTL), which is dedicated to research activities [11]. The production of the ^{43}Sc radioisotope is performed via $^{46}Ti(p,\alpha)^{43}Sc$ reaction. It has a relatively long half-life of 3.89 hours as well as the desired decay properties such as a low positron energy of 1.2 MeV with the decay probability of 71%, and a low gamma ray energy of 373 keV with the decay probability of 22.5%. While its long half-life enables observations of the cell abnormalities in detail, high-resolution images can be acquired with its sufficient decay conditions.

The production takes place in the Bern cyclotron by performing the $^{46}Ti(p,\alpha)^{43}Sc$ reaction. Twenty-five different TiO_2 targets are prepared with a high enrichment rate of 96.9%. Such a high rate prevents the undesired interactions of possible sub-particles within the matter. The atomic mass of ^{46}Ti radioisotope is 45.9526 g/mol, as the molar mass of TiO_2 is 77.9 g/mol. They are bombarded by proton beams at different energy values to obtain the ^{43}Sc radioisotopes. Although the cyclotron has a unique energy value of 18 MeV, the degradation is performed to make irradiations possible at a wide energy range. Various numbers of Al foils, each has a thickness of 100 μm, are placed in front of the target as an energy degrader. Aluminum has a good thermal

conductivity of 2.37 $W.cm^{-1}.C^{-1}$ that decreases the cooling time of the target. In addition, 31.86 MeV of energy threshold for the proton activation is quite high to lower the possibility of any interactions during the irradiation process. The degradation is simulated by SRIM Monte Carlo code [47]. The minimum beam energy on the target obtained by the simulation is 0.77 MeV. This value is high enough to match with the threshold energy of the corresponding reaction at 3.142 MeV [25]. After the irradiation completed, activity is measured to calculate the cross-section value of the ^{43}Sc radioisotope. The measurement is accomplished with the HPGe detector installed in the Bern laboratory. The irradiated targets are placed into the germanium detector in order to observe a gamma ray emission peak of ^{43}Sc at 373 keV. The net peak area for the emission is obtained from the gamma ray spectroscopy, and is used for the cross-section calculation. Other important factors that affect the calculation are the beam flux, the irradiation area, duration of the cooling and the measurement processes, and calibration of the detector. The cross-section data are compared to both the experimental values (EXFOR), and the theoretical database (TENDL-2015). The result agrees with TENDL database up to 13 MeV, and it approaches EXFOR data after that point. The cross-section has a peak at $40.98 \mp 1.7506\ mb$ and a minimum at $0.75 \mp 0.0375\ mb$. In other words, its maximum production yield is at 16.2 MeV, as the minimum one is observed at 8.34 MeV. The theoretical simulations, and the experimental data show that the maximum cross-section value of the present measurement remains between the maximum values of these databases. In case of this study, it is possible to reach the maximum value of TENDL at $31.42 \mp 1.6494\ mb$ with the energy of 13.5 MeV.

Apart from the ^{43}Sc production, the solid target station, which has been recently installed at the Bern Laboratory, is conceived to obtain new radioisotopes with different kinematics. Within this framework, the ^{48}V radioisotope is produced via the $^{nat}Ti(p,x)^{48}V$ reaction. Due to its decay properties, ^{48}V has two gamma ray peak at 983 keV, and at 1312 keV. As a result of the first irradiation test, two cross-section values are observed at these energy points and compared to the reference cross-section values of IAEA. The obtained result is almost same with the reference data, and has a peak at 389 mb with the energy of 11.2 MeV. Further measurements are required to decide the maximum yield of the ^{48}V radioisotope.

The production cross-sections of both ^{43}Sc, and ^{48}V state that they can be assumed as the promising candidates and can easily replace the conventional PET radioisotopes. The yield of the production can be increased by optimizing the determinant factors in the calculation. The calibration of the HPGe detector should be considered as one of these main factors, and performed regularly. The Bern medical cyclotron laboratory allows for the further measurements of the cross-sections as well as the cutting-edge researches.

REFERENCES

[1] M. Pillai *et al.*, "Cyclotron produced radionuclides: Principle and practice," *Technical reports series 465, International Atomic Energy Agency*, 2008.

[2] K. Gschneidner *et al.*, "SCANDIUM:its ocurrence, chemistry, physics, metallurgy, biology, and technology," *Academic Press*, 1975.

[3] "Lecture 5: Tomographic nuclear systems: SPECT," *http://courses.washington.edu/bioen508/Lecture5-A-SPECT.pdf*. Accessed: 30/04/2017.

[4] L. Goldman, "Principles of CT and CT technology," *The Journal of Nuclear Medicine Technology*, vol. 35, pp. 115–128, 2007.

[5] A. Berger, "Magnetic resonance imaging," *BMJ: British Medical Journal*, vol. 324, p. 35, 2002.

[6] T. Bateman, "Advantages and disadvantages of PET and SPECT in a busy clinical practice," *Journal of Nuclear Cardiology*, vol. 19, pp. 3–11, 2012.

[7] "PET chemist." https://petchemist.wordpress.com/, April 2016. Accessed: 04/05/2017.

[8] D. Papathanassiou *et al.*, "Positron emission tomography in oncology: Present and future of PET and PET/CT," *Critical Reviews in Oncology/Hematology*, vol. 72, pp. 239–254, 2009.

[9] D. Townsend, "Combined PET/CT: the historical perspective," *Semin Ultrasound CT MR*, vol. 29, pp. 232–235, 2008.

[10] "The history of the PET-CT scanner." https://www.amberusa.com/blog/the-history-of-the-pet-ct\discretionary{-}{}{}scanner, July 2016. Accessed: 01/06/2017.

[11] S. Braccini, "Particle accelerators and detectors for medical diagnostics and therapy," *Habilitation thesis, University of Bern*, 2013.

[12] "Nuclear chemistry." http://faculty.sdmiramar.edu/fgarces/zCourse/All_Year/Ch100_OL/aMy_FileLec/04OL_LecNotes_Ch100/04_NuclearChem/401_NukeChem/401_NukeChem.htm. Accessed: 24/11/2016.

[13] A. Reina, "Medical cyclotron," in *12 Chapters on Nuclear Medicine*, InTech, December 2011.

[14] S. Braccini, "The solid target station of the bern cyclotron laboratory," *Power Point slides*, April 2017.

[15] J. Brownlee, "The radiochemistry of vanadium," *National Academy of Sciences*, vol. 3022, p. 51, December 1960.

[16] S. Braccini *et al.*, "Science with a medical pet cyclotron," *CERN Courier*, vol. 56, pp. 21–22, 2016.

[17] A. Mandal, "Nuclear medicine techniques." `http://www.news-medical.net/health/Nuclear-Medicine-Techniques.aspx`. Accessed: 29/04/2017.

[18] "Preclinical PET/CT and SPECT/CT." `http://www.med.lu.se/bioimaging_center/lbic_platforms/preclinical_nuclear_medicine_pet_spect_ct/basic_principles`. Accessed: 01/05/2017.

[19] T. Ruth, "The uses of radiotracers in the life sciences," *Rep. Prog. Phys.*, vol. 72, 2009.

[20] A. Buck *et al.*, "SPECT/CT," *The Journal of Nuclear Medicine*, vol. 49, pp. 1305–1319, 2008.

[21] C. Hoh *et al.*, "PET in oncology: will it replace the other modalities?," *Semin Nucl Med.*, vol. 27, pp. 94–106, 1997.

[22] S. Ziegler, "Positron emission tomography: Principles, technology, and recent developments," *Nuclear Physics A*, vol. 752, pp. 679c–687c, 2005.

[23] E. Keigo *et al.*, "PET and PET/CT using 18F-FDG in the diagnosis and management of cancer patients," *Int. J. Clin. Oncol.*, vol. 11, pp. 286–296, 2006.

[24] C. Duchemin *et al.*, "Production of scandium-44m and scandium-44g with deuterons on calcium-44: cross section measurements and production yield calculations," *Physics in Medicine & Biology*, vol. 61, pp. 6856–6857, 2016.

[25] "TENDL: TALYS-based evaluated nuclear data library, 2015," *`https://tendl.web.psi.ch/tendl_2015/proton_file/Ti/046/xs/xs000001.tot`*. Accessed: 24/04/2017.

[26] M. Daube-Witherspoon *et al.*, "Developments in instrumentation for emission computed tomography," *Seminars in Nuclear Medicine*, vol. 33, pp. 28–41, 2003.

[27] E. Lawrence *et al.*, "The production of high speed light ions without the use of high voltages," *Phys. Rev. Lett*, vol. 40, pp. 19–35, 1932.

[28] L. Nemenov, "The history of the development of the cyclotron over fifty years(1930-1980)," *Usp. Fiz. Nauk*, vol. 133, pp. 525–541, 1981.

[29] P. Schmor, "Review of cyclotrons used in the production of radioisotopes for biomedical applications," *Proceedings of 19th Int. Conf. on Cyc*, vol. 133, pp. 525–541, 2010.

[30] A. W. Chao and W. Chou, "Reviews of accelerator science and technology," WORLD SCIENTIFIC, February 2012.

[31] S. Braccini *et al.*, "The new bern cyclotron laboratory for radioisotope production and research," *Conf. Proc.*, vol. C110904, pp. 3619–3621, September 2011.

[32] D. Clark, "Accelerators for nuclear physics," *Reports on Progress in Physics*, vol. 35, pp. 1007–1075, 2010.

[33] J. Cockcroft, "The cyclotron and betatron," *Journal of Scientific Instruments*, vol. 21, p. 189, 1944.

[34] J. Botman *et al.*, "Extraction from cyclotrons," *In CERN Accelerator School*, pp. 169–185, 1994.

[35] J. Ristić-Djurović, "Stripping extraction of positive ions from a cyclotron," *Physical Review Special Topics - Accelerators and Beams*, vol. 4, p. 123501, 2001.

[36] W. A. Loveland *et al.*, "Nuclear reactions," in *Modern Nuclear Chemistry*, pp. 247–303, John Wiley & Sons, Inc., March 2017.

[37] M. Mostafaei, "Measurement of Sc-43 production croos-section with a medical cyclotron," *Master thesis*, 2015.

[38] "Imaging processing and analysis in java." `https://imagej.nih.gov/ij/`. Accessed: 15/04/2017.

[39] S. Braccini *et al.*, "A beam monitor detector based on silica doped and optical fibres," *Journal of Instrumentation*, vol. 44, 2012.

[40] M. Khandaker, "High purity germanium detector in gamma-ray spectrometry," *IJFPS*, vol. 1, pp. 42–46, 2011.

[41] A. Patil, "Dead time and count loss determination for radiation detection systems in high count rate applications," *Doctoral Dissertations*, vol. Paper 2148, 2010.

[42] R. Njinga *et al.*, "Calibration of the high purity germanium gamma-ray spectrometer in cert, abu zaria, nigeria," *Modern Instrumentation*, vol. 4, pp. 11–17, 2015.

[43] "What do we mean by 'cross section' in particle physics?." `http://cms.web.cern.ch/news/what-do-we-mean-cross-section-particle-physics`, March 2013. Accessed: 27/03/2017.

[44] "TENDL: TALYS-based evaluated nuclear data library, 2015." `https://tendl.web.psi.ch/tendl_2015/tendl2015.html`. Accessed: 24/04/2017.

[45] "EXFOR: Experimental nuclear reaction data." `https://www-nds.iaea.org/exfor/exfor.htm`. Accessed: 24/04/2017.

[46] "Charged particle cross-section database for medical radioisotope production diagnostic radioisotopes and monitor reactions," *Final report of a co-ordinated research project*, May 2011.

[47] "SRIM-the stopping and range of ions in matter." `http://www.srim.org/`. Accessed: 14/04/2017.

APPENDIX A

THE DATA USED FOR THE CROSS-SECTION MEASUREMENTS

In this section, all numeric values used for calculation of the activity, and for measurement of the cross-section are listed. Table 1 includes the all values obtained by the energy degradation. Alterations of the proton beam energies with regarding aluminum foil thicknesses, and their uncertainties may be found on this table. In table 2, relation between the cooling time of the irradiated targets, and dead time of the corresponding measurements obtained with the HPGe detector are represented. Furthermore, the energy degradation results, masses of the different targets with their uncertainties, error on the HPGe detector, activity measurement of each irradiation are used for the cross-section calculations of ^{43}Sc and available in Table 3. The result of the current study are compared with the EXFOR and the TENDL database. The database are presented up to the energies of 23 MeV, and 30 MeV, respectively in Table 4. As a result of the irradiation performed by the Bern solid target station, the ^{48}V radioisotope is produced. The theoretical cross-section data for this production are provided by IAEA and represented in Table 5. On the other hand, Figure 1 and Figure 2 are the detailed reports of the gamma ray spectrum observed for both ^{43}Sc, and ^{48}V.

TableA.1: Cyclotron energy values regarding different aluminum thicknesses

thickness (μm)	thickness uncertainty (μm)	energy (MeV)	energy uncertainty (MeV)	thickness (-10%) (μm)	energy (MeV)	energy uncertainty (MeV)	thickness (+10%) (μm)	energy (MeV)	energy uncertainty (MeV)
100	10	17.4	0.04	90	17.47	0.04	110	17.3	0.05
200	20	16.8	0.06	180	16.9	0.07	220	16.7	0.06
300	30	16.2	0.08	270	16.38	0.06	330	16	0.09
400	40	15.6	0.09	360	15.8	0.09	440	15.29	0.10
500	50	14.9	0.11	450	15.2	0.10	550	14.55	0.12
600	60	14.2	0.12	540	14.6	0.13	660	13.78	0.14
700	70	13.5	0.13	630	13.9	0.13	770	12.97	0.16
800	80	12.75	0.15	720	13.3	0.14	880	12.13	0.19
900	90	11.9	0.17	810	12.67	0.15	990	11.23	0.19
1000	100	11.1	0.23	900	11.98	0.17	1100	10.29	0.21
1100	110	10.3	0.20	990	11.23	0.19	1210	9.25	0.22
1200	120	9.35	0.24	1080	10.47	0.21	1320	8.13	0.26
1300	130	8.34	0.30	1170	9.64	0.22	1430	6.86	0.30
1400	140	7.21	0.30	1260	8.75	0.23	1540	5.41	0.36
1500	150	5.96	0.34	1350	7.80	0.26	1650	3.54	0.49
1600	160	4.46	0.41	1440	6.75	0.31	1760	1.08	0.61
1700	170	2.40	0.66	1530	5.54	0.34	-	-	-
1800	180	0.77	0.45	1620	4.12	0.44	-	-	-
1900	-	-	-	1710	2.13	0.70	-	-	-
2000	-	-	-	1800	0.79	0.47	-	-	

TableA.2: The relation between the cooling time and the dead time

cooling time (t_c) [min]	dead time [%]
18	6.25
20	4.81
22	6.79
23	4.30
24	5.83
25	3.25
28	1.73
30	1.54
32	0.43
35	1.34

```
Peak Locate Analysis Report             12.11.2015 15:06:00        Page  1

*************************************************************************
*****             P E A K   L O C A T E   R E P O R T               *****
*************************************************************************

     Detector Name:  GR2019
     Sample Title:   Ti1_500um
               Peak Locate Performed on:  12.11.2015 15:06:00
               Peak Locate From Channel:      1
               Peak Locate To Channel:     4096
               Peak Search Sensitivity:    20.00

     Peak   Centroid    Centroid     Energy       Peak
      No.    Channel   Uncertainty   (keV)    Significance

       1      586.40      0.0976      372.70      63.21
       2      803.57      0.0452      510.84     179.77

? = Adjacent peak noted

Errors quoted at  1.000 sigma
Peak Analysis Report             12.11.2015 15:06:19              Page  1


*************************************************************************
*****          P E A K   A N A L Y S I S   R E P O R T             *****
*************************************************************************

     Detector Name:  GR2019
     Sample Title:   Ti1_500um
     Peak Analysis Performed on:  12.11.2015 15:06:19
               Peak Analysis From Channel:      1
               Peak Analysis To Channel:     4096

   Peak  ROI  ROI    Peak    Energy   FWHM  Net Peak  Net Area  Continuum
    No. start end  centroid   (keV)   (keV)  Area     Uncert.    Counts

    1   582-  590   586.40   372.70   1.44  2.76E+004  275.24   1.93E+004
    2   799-  807   803.57   510.84   2.72  1.04E+006 1074.01   4.37E+004

M = First peak in a multiplet region
m = Other peak in a multiplet region
F = Fitted singlet

Errors quoted at  1.000 sigma
Background Subtract Report              12.11.2015 15:06:30         Page  1

*************************************************************************
*****        B A C K G R O U N D  S U B T R A C T  R E P O R T      *****
*************************************************************************

     Detector Name:  GR2019
     Sample Title:   Ti1_500um
     Peak Analysis Performed on:  12.11.2015 15:06:00

     Env. Background File:     C:\GENIE2K\CAMFILES\GR2019-GammaSpectra

 Peak  Energy  Original Orig. Area  Ambient    Backgr.  Subtracted  Subtracted
   No. (keV)     Area     Uncert.  Background  Uncert.     Area       Uncert.

    1   372.70  2.76E+004  275.24                        2.76E+004  2.75E+002
    2   510.84  1.04E+006 1074.01   6.38E+000  1.70E-001  1.04E+006  1.07E+003


M = First peak in a multiplet region
m = Other peak in a multiplet region
```

Figure A.1: Peak analysis report for the gamma emission line of ^{43}Sc at 14.9 MeV

TableA.3: All data required for the cross-section calculation of the ^{43}Sc radioisotope

Al thickness (μm)	Energy (MeV)	Energy uncertainty (MeV)	Cross section (mb)	Cross section uncertainty (mb)	Activity (Bq)	Error HPGe [%]	Mass (g)	Error mass [%]
0	18.34	0.01	34.96	1.3984	1.93E+03	0.000	3.30E-3	0.0400
100	17.4	0.04	40.68	1.8348	1.99E+03	0.0120	2.30E-3	0.0435
300	16.2	0.08	40.98	1.7506	1.66E+03	0.0150	2.50E-3	0.0400
400	15.93	0.09	39.75	1.6490	2.12E+03	0.0110	2.50E-3	0.0400
600	14.2	0.12	35.94	1.6520	1.43E+03	0.0150	2.30E-3	0.0435
700	13.5	0.13	31.42	1.6494	1.30E+03	0.0160	2.00E-3	0.0500
800	12.75	0.15	25.37	1.234	1.03E+03	0.0100	2.10E-3	0.0476
900	11.9	0.17	19.1	1.0285	8.32E+02	0.0200	2.00E-3	0.0500
1000	11.1	0.17	17.98	0.848	9.55E+02	0.0250	2.50E-3	0.0400
1100	10.3	0.20	11.03	0.470	4.74E+02	0.0300	3.30E-3	0.0303
1200	9.35	0.24	3.43	0.2330	1.63E+02	0.0550	2.10E-3	0.0400
1300	8.34	0.30	0.75	0.0375	4.05E+01	0.000	2.10E-3	0.450

TableA.4: Comparison of the EXFOR and the TENDL database with the present study

EXFOR [MeV]	EXFOR cross-section [mb]	TENDL [MeV]	TENDL cross-section [mb]	Energy of this study [MeV]	Cross-section of this study [mb]
7.70E+00	4.8∓0.48	1.00E+00	0.00E+00	17.9∓0.02	40.98∓1.75
8.60E+00	19∓1.9	2.00E+00	0.00E+00	16.1∓0.08	35.94∓1.65
9.50E+00	19∓1.9	3.00E+00	0.00E+00	14.1∓0.12	19.1∓1.03
1.04E+01	27∓2.7	4.00E+00	0.00E+00	11.9∓0.17	3.46∓0.233
1.13E+01	36∓3.6	5.00E+00	3.74E-09	9.35∓0.24	40.67∓1.83
1.21E+01	35∓3.5	6.00E+00	7.90E-05	17.4∓0.04	39.75∓1.65
1.28E+01	39∓3.9	7.00E+00	1.31E-02	15.6∓0.09	31.42∓1.65
1.38E+01	43∓4.3	8.00E+00	3.13E-01	13.5∓0.13	25.37∓1.23
1.48E+01	46∓4.6	9.00E+00	2.20E+00	12.8∓0.15	17.84∓0.848
1.58E+01	45∓4.5	1.00E+01	7.42E+00	11.1∓0.23	11.03∓0.470
1.67E+01	41∓4.1	1.10E+01	1.48E+01	10.3∓0.2	34.96∓1.4
1.75E+01	43∓4.3	1.20E+01	2.11E+01	18∓0.02	0.75∓0.0375
1.83E+01	41∓4.1	1.30E+01	2.56E+01	8.95∓0.25	
1.93E+01	39∓3.9	1.40E+01	2.86E+01		
2.03E+01	29∓2.9	1.50E+01	3.06E+01		
2.14E+01	24∓2.4	1.60E+01	3.08E+01		
2.22E+01	19∓1.9	1.70E+01	2.82E+01		
2.31E+01	16∓1.6	1.80E+01	2.35E+01		
		1.90E+01	1.80E+01		
		2.00E+01	1.29E+01		
		2.20E+01	6.26E+00		
		2.40E+01	3.37E+00		
		2.60E+01	2.16E+00		
		2.80E+01	1.55E+00		
		3.00E+01	1.20E+00		

Peak Locate Analysis Report 08.11.2016 17:07:06 Page 1

****

***** P E A K L O C A T E R E P O R T *****

****

Detector Name: GR2019
Sample Title: NatTi_ST_test1
Peak Locate Performed on: 08.11.2016 17:07:06
Peak Locate From Channel: 1
Peak Locate To Channel: 4096
Peak Search Sensitivity: 3.75

Peak No.	Centroid Channel	Centroid Uncertainty	Energy (keV)	Peak Significance
1	586.26	0.4140	372.61	4.29
2	803.19	0.0723	510.60	81.31
3	1483.58	0.3295	943.40	4.88
4	1545.58	0.1544	982.84	20.83
5	1817.96	0.2096	1156.10	10.25
6	2061.97	0.1520	1311.32	19.40

? = Adjacent peak noted

Errors quoted at 1.000 sigma

Peak Analysis Report 08.11.2016 17:07:11 Page 1

****

***** P E A K A N A L Y S I S R E P O R T *****

****

Detector Name: GR2019
Sample Title: NatTi_ST_test1
Peak Analysis Performed on: 08.11.2016 17:07:11
Peak Analysis From Channel: 1
Peak Analysis To Channel: 4096

Peak No.	ROI start	ROI end	Peak centroid	Energy (keV)	FWHM (keV)	Net Peak Area	Net Area Uncert.	Continuum Counts
1	582-	590	586.26	372.61	1.22	2.37E+002	93.51	3.38E+003
2	798-	807	803.19	510.60	2.52	1.59E+005	418.17	5.86E+003
3	1478-	1488	1483.58	943.40	1.62	2.09E+002	35.36	4.37E+002
4	1540-	1550	1545.58	982.84	1.74	2.05E+003	55.26	4.24E+002
5	1812-	1823	1817.96	1156.10	1.99	5.34E+002	33.17	2.26E+002
6	2056-	2067	2061.97	1311.32	2.00	1.46E+003	41.77	1.15E+002

M = First peak in a multiplet region
m = Other peak in a multiplet region
F = Fitted singlet

Errors quoted at 1.000 sigma

Background Subtract Report 08.11.2016 17:07:17 Page 1

No background subtract performed on this spectrum.

Figure A.2: Peak analysis report for the gamma emission line of ^{48}V at 11.2 MeV

TableA.5: Recommended cross-sections for the $^{nat}Ti(p,x)^{48}V$ reaction provided by IAEA

Energy [MeV]	Cross-section [mb]	Energy [MeV]	Cross-section [mb]	Energy [MeV]	Cross-section [mb]	Energy [MeV]	Cross-section [mb]
5.0	0.5	11	370	17.5	146	24.0	50.7
5.5	73.9	11.5	378	18.0	129	24.5	48.4
6	145	12.0	382	18.5	115	25.0	46.3
6.5	196	12.5	382	19.0	104	25.5	44.3
7	237	13.0	375	19.5	93.9	26.0	42.6
7.5	270	13.5	361	20.0	85.7	26.5	41.0
8.0	295	14.0	338	20.5	78.8	27.0	39.6
8.5	314	14.5	310	21	72.9	27.5	38.2
9.0	329	15.0	279	22	63.4	28	37.0
9.5	341	15.5	247	22.5	59.6	28.5	35.8
10.0	352	16.5	216	23.0	56.3	29.0	34.8
10.5	362	17.0	189	23.5	53.3	29.5	33.7